AD_____

Award Number: W81XWH-10-1-0132

TITLE: Metallated DNA Aptamers for Prostate Cancer Treatment

PRINCIPAL INVESTIGATOR: William H. Gmeiner

CONTRACTING ORGANIZATION: Wake Forest University School of Medicine
Winston-Salem, NC 27157

REPORT DATE: March 2013

TYPE OF REPORT: Final Report

PREPARED FOR: U.S. Army Medical Research and Materiel Command
Fort Detrick, Maryland 21702-5012

REPORT DOCUMENTATION PAGE

Form Approved
OMB No. 0704-0188

1. REPORT DATE	2. REPORT TYPE	3. DATES COVERED
March 2013	Final Report	15 February 2010- 14 February 2013

4. TITLE AND SUBTITLE
Metallated DNA Aptamers for Prostate Cancer Treatment

5a. CONTRACT NUMBER

5b. GRANT NUMBER
W81XWH-10-1-0132

5c. PROGRAM ELEMENT NUMBER

6. AUTHOR(S)
William H. Gmeiner

5d. PROJECT NUMBER

5e. TASK NUMBER

5f. WORK UNIT NUMBER

7. PERFORMING ORGANIZATION NAME(S) AND ADDRESS(ES)
Wake Forest University School of Medicine
Winston-Salem, NC 27157

8. PERFORMING ORGANIZATION REPORT NUMBER

9. SPONSORING / MONITORING AGENCY NAME(S) AND ADDRESS(ES)
U.S. Army Medical Research and Materiel Command
Fort Detrick, Maryland 21702-5012

10. SPONSOR/MONITOR'S ACRONYM(S)

11. SPONSOR/MONITOR'S REPORT NUMBER(S)

12. DISTRIBUTION / AVAILABILITY STATEMENT
Approved for Public Release; Distribution Unlimited

13. SUPPLEMENTARY NOTES

14. ABSTRACT
The purpose of this project is to develop DNA aptamer complexes that are selectively cytotoxic to PSMA+ prostate cancer (PCa) cells. Our studies showed Zn2+ is cytotoxic to prostate cancer cells and also sensitizes PCa cells to chemotherapy. We developed a new DNA motif for Zn2+ delivery. We also developed a new chemical strategy for delivering the cytotoxic drug doxorubicin to cancer cells. We have demonstrated that our novel dimeric aptamer complexes are selectively internalized by PSMA+ prostate cancer cells and have demonstrated selective cytotoxicity with delivery of doxorubicin. We also developed a new nanoparticle (NP) composed of porphyrin and DNA and demonstrated that this NP was cytotoxic to bladder cancer cells in vitro, was non-toxic in vivo, and displayed strong anti-tumor activity in vivo. The aptamer complexes and the NPs we developed in this project are highly selective and highly active agents that have the potential to markedly improve chemotherapy for treatment of advanced prostate cancer.

15. SUBJECT TERMS-

Prostate cancer, DNA-metal interactions, Zn2+, structural biology

16. SECURITY CLASSIFICATION OF:			17. LIMITATION OF ABSTRACT	18. NUMBER OF PAGES	19a. NAME OF RESPONSIBLE PERSON
a. REPORT	b. ABSTRACT	c. THIS PAGE			USAMRMC
U	U	U	UU		19b. TELEPHONE NUMBER *(include area code)*

Table of Contents

INTRODUCTION: The project "Metallated DNA Aptamers for Prostate Cancer Treatment" provides information on a novel therapeutic approach for prostate cancer treatment in which Zn2+ chelates are delivered specifically to prostate cancer cells using DNA aptamers that bind to prostate specific membrane antigen (PSMA). Our preliminary data indicated that chelated Zn2+ (Zn2+-pyrithone) was cytotoxic towards human prostate cancer cells and that Zn2+-pyrithione enhanced the cytotoxicity of FdUMP[10], a novel polymeric fluoropyrimidine compound that is under investigation in Dr. Gmeiner's lab at WFSM for the treatment of prostate cancer and other malignancies. The project involves developing new DNA aptamers that bind to PSMA, incorporating Zn2+-chelating DNA structural elements proximal to the PSMA-binding sequence, and forming aptamer-targeted Zn2+:DNA complexes. The resulting modified DNA aptamers are then used to form a dimeric aptamer complex composed of two monomeric aptamers. Dimerization is accomplished by including a polydA tail in one aptamer complex and a polydT tail in a second aptamer complex, with dimerization occurring by Watson-Crick base pair formation. Cytotoxicity is engineered into the dimeric aptamer complex by inclusion of 5-fluoro-2'-deoxyuridine-5'-O-monophosphate (FdUMP) in place of dT in the dimerization motif or by covalent conjugation with the anti-cancer drug doxorubicin. We recently demonstrated that stretches of consecutive FdU nucleotides create a unique major groove binding motif for Zn2+ (Ghosh et al., 2011; Ghosh et al., 2012 - appendix #1). This novel mode of Zn2+ binding will be used for creating the dimeric aptamer complexes. The resulting dimeric aptamer complexes will be evaluated for cytotoxicity towards prostate cancer cells in tissue culture and towards prostate cancer xenografts in nude mice as an animal model of human prostate cancer. The long-term goal of this research is to develop a highly specific, well-tolerated, and highly potent therapeutic approach for treatment of advanced prostate cancer.

BODY:

Revised Aim 1: ***Evaluate the utility of DNA sequences containing consecutive FdU nucleotides for intracellular delivery of Zn2+ to PSMA+ PCa cells*****. (Y1:Q1-4; Y2: Q1-3).**

Revised Task 1.A. Synthesize DNA hairpins with sequences containing FdU nucleotides and identify conditions useful for Zn2+ complex formation under physiological conditions. The stem region of the hairpin provides a model for the dimerization motif that will be used to create dimeric aptamer complexes.

a. Synthesize DNA hairpins with consecutive FdU nucleotides at the 3'-terminus, 5'-terminus, or alternating FdU-dA nucleotides for the stem region. **DNA hairpins will be chemically synthesized with FdU nucleotides site-specifically included either consecutively near the 5'- or 3'-terminus or alternating with dA nucleotides in the stem region**.

We have synthesized DNA hairpins having the properties required for these studies. A complete description of the synthesis, purification and spectral characterization of these DNA hairpins was

included in our recent publication that was reported in the previous annual progress report (Ghosh et al., 2011).

b. Use spectroscopic methods (CD, NMR, fluorescence) to demonstrate Zn2+ complex formation and evaluate the role of the FdU sequence in promoting Zn2+ complex formation.

We have completed spectroscopic evaluation and demonstrated Zn2+ complex formation occurs and that consecutive FdU nucleotides are required for Zn2+ complexes to form and have reported these novel findings (Ghosh et al., 2011).

c. Evaluate binding of netropsin to DNA hairpins with stems consisting of consecutive FdU and consecutive dA nucleotides and determine if netropsin binding facilitates Zn2+ complexation.

We recently completed 2D NMR and other studies demonstrating that netropsin binds to DNA hairpin sequences with stems consisting of consecutive FdU-dA base pairs (Ghosh et al., 2012 – appendix #1). We have also demonstrated that netropsin binding to the 3'-FdU DNA hairpin sequence facilitates Zn2+ complexation. This work is highly novel in two fundamental aspects: i) these are the first studies demonstrating that netropsin binds DNA sequences with FdU-dA base pairs; ii) these are the first studies to demonstrate simultaneous binding in the minor and major grooves of DNA in order to deliver a therapeutic payload for cancer treatment.

This complex is highly novel from a structural biology viewpoint and it is also very important for this project because it demonstrates the feasibility of using this DNA structural motif to create the dimeric aptamer complexes that are the long-range goal of these studies. To further assess the therapeutic potential of this complex we have performed cytotoxicity assays with prostate cancer cells. Importantly, our studies have shown that the netropsin-stabilized Zn2+/DNA complexes are highly cytotoxic towards PC3 prostate cancer cells (Ghosh et al., 2012) indicating this motif is likely to be useful in creating the dimeric aptamer complexes that are the goal of these studies.

d. Evaluate FdU-dG base pair formation and determine if Zn2+ complexes with duplex DNA including FdU-dG base pairs are more stable under physiological conditions than duplex DNA including FdU-dA base pairs.

We have undertaken preliminary experiments with a DNA hairpin having a stem consisting of FdU-dG base pairs. The impetus for these studies is that the complexes involving A-FdU base pairs required pH slightly above physiological for long-term stability and thus were not ideal for *in vivo* delivery of therapeutics which is the long-term goal of these studies. G-FdU base pairs can form two hydrogen bonds even when FdU is deprotonated and we thought that this might allow such complexes to form and persist at physiological pH.

Although some of our studies demonstrated that the G-FdU sequences displayed the targeted properties, these sequences were not sufficiently stable for further development. We have re-designed the duplex DNA used for forming the dimeric aptamer complexes to included G-C nucleotides at the termini and A-T base pairs in the interior. The A-T base pairs may be substituted with A-FdU for cytotoxic nucleotide delivery while the G-C base pairs provide additional stability and provide a site for covalent attachment of Doxorubicin which is cytotoxic to prostate cancer cells. Our studies established the stability of this sequence motif in the context of the dimeric aptamer (Figure 1).

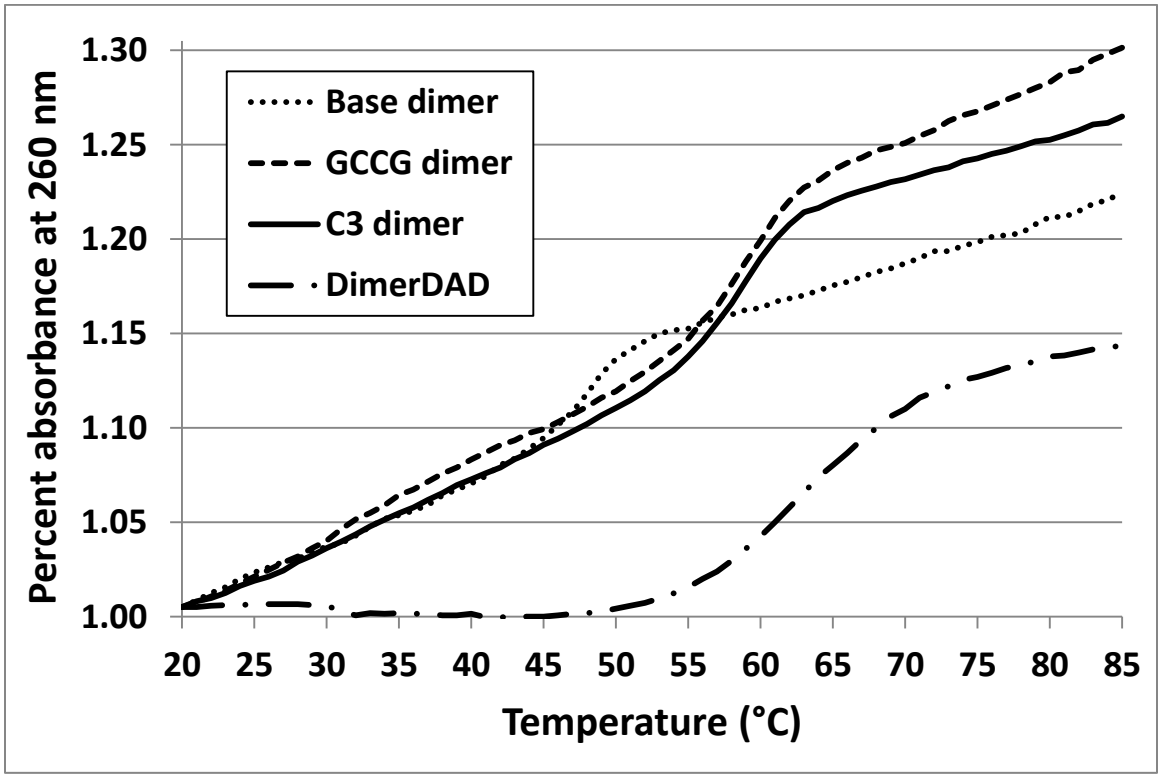

Figure 1. PSMA-specific aptamer dimer melting curve. The dA and dT tailed aptamers were resuspended in DEPC treated H_2O and mixed 1:1, heated up to 95°C for 2 min, gradually cooled down to 70°C for 2 min, and room temperature for 10 min, and stored at 4°C overnight to enable the proper formation of secondary structure while allowing the aptamers to anneal through their dA and dT tails. PSMA-specific aptamer dimer was diluted to 1 uM in DPBS and melting curve between 20-84°C was generated by measuring absorbance at 260 nm. **Base dimer:** Forty-eight base long aptamers were synthesized with 16 base long tails of either adenine (dA[16]) or thymine (dT[16]) on their 3' ends. **GCCG dimer:** The 16 base long tail is extended to 24 bases by adding doxorubicin binding motifs of GCCG/CGGC to the front and back of the tail. **C3 dimer:** A three-carbon spacer (C3) was placed between the 48 base long aptamer and the 24 base long tail of GCCG dimer to provide an added flexibility to the dimer molecule. **DimerDAD:** The GCCG dimer covalently modified with four Dox linked through a hydrolysable methylene bridge.

Task 1.B. Evaluate the binding and internalization of these aptamer conjugates into prostate cancer cells and determine to what extent specific internalization is achieved into $PSMA^+$ cells. (Y1:Q3)

a. Cellular binding by fluorescence microscopy. The QST16 and QSA16 monomeric aptamers will be synthesized with fluorescent probes at their 5'-terminii. Binding to $PSMA^+$ (e.g. C4-2) and $PSMA^-$ (e.g. PC3) as monomers and as a dimer will be evaluated by fluorescence microscopy. (Y1: Q3)

We performed this study previously using the dT16 and dA16 aptamer complexes derived from the $SZTI_{PSMA01}$ aptamer. We did not include the quadruplex forming sequence element as we were in the process of developing the new Zn2+-binding motif. These studies showed strong binding to both PSMA+ and PSMA- cells. Thus, we did not have the required selectivity for PSMA+ cells and we re-initialized the SELEX procedure to identify a new DNA aptamer to PSMA.

We re-initialized the systematic evolution of ligands through an exponential enrichment (SELEX) procedure to identify a new DNA aptamer to PSMA. We completed the SELEX procedure and identified the following DNA sequence as having high affinity for PSMA.

5'-dGGCCATAAGCGGTCACACAATCCCGTGATTCGCCTGCTA

Although we obtained some apparently promising results with this sequence, the post-doctoral fellow working on the project was terminated (Dr. Tuya Sharkhuu) and the new post-doctoral fellow working on this project (Dr. Olcay Boyacioglu) was unable to re-produce the results. We were however, able to demonstrate that $SZTI_{PSMA01}$ aptamer, in the context of the dimeric aptamer complex, had the desired selectivity for $PSMA^+$ C4-2 cells relative to PSMA-null PC3 cells (Figure 2). We are completing studies with the $SZTI_{PSMA01}$ dimeric aptamer complex (DAC) and have a manuscript in preparation (appendix #2) that we plan to submit within the next 30 days. We are also preparing a manuscript on the preparation of doxorubicin conjugates of a DNA hairpin using this technology (appendix #3).

b. Effects of Zn2+ complexation on cellular binding. The QST16 and QSA16 aptamer conjugates will form complexes with ZnPc and the effects of complex formation on cellular binding will be investigated using fluorescence microscopy. (Y1: Q4).

Our preliminary studies indicated that dT-dA base pairing does not interfere with cellular binding or uptake. We have completed studies in which we have used the 24 nucleotide sequence $GCGCA_{16}GCGC$ and corresponding sequence $GCGCT_{16}GCGC$ to form the dimeric complex. Although we can deliver Zn2+ with this sequence we have focused on delivering Doxorubicin for proof of principle studies. We have made this change for two reasons: 1) Our studies with Zn2+ in combination with FdUMP[10] have become more complex (see report for Aim 2); and 2) Doxorubicin can be selectively bound to this sequence and we are able to kill prostate cancer cells

very selectively (appendix #2). Thus, using this approach we have developed a novel strategy for selective delivery of doxorubicin to prostate cancer cells which has strong therapeutic potential.

c. Evaluate cellular internalization of aptamer complexes using confocal microscopy and flow cytometry. The QST16 and QSA16 monomeric aptamer conjugates with fluorescent probes will be evaluated for cellular internalization into $PSMA^+$ and $PSMA^-$ cells using confocal microscopy and flow cytometry. The dimeric complex will be similarly analyzed. (Y1: Q4)

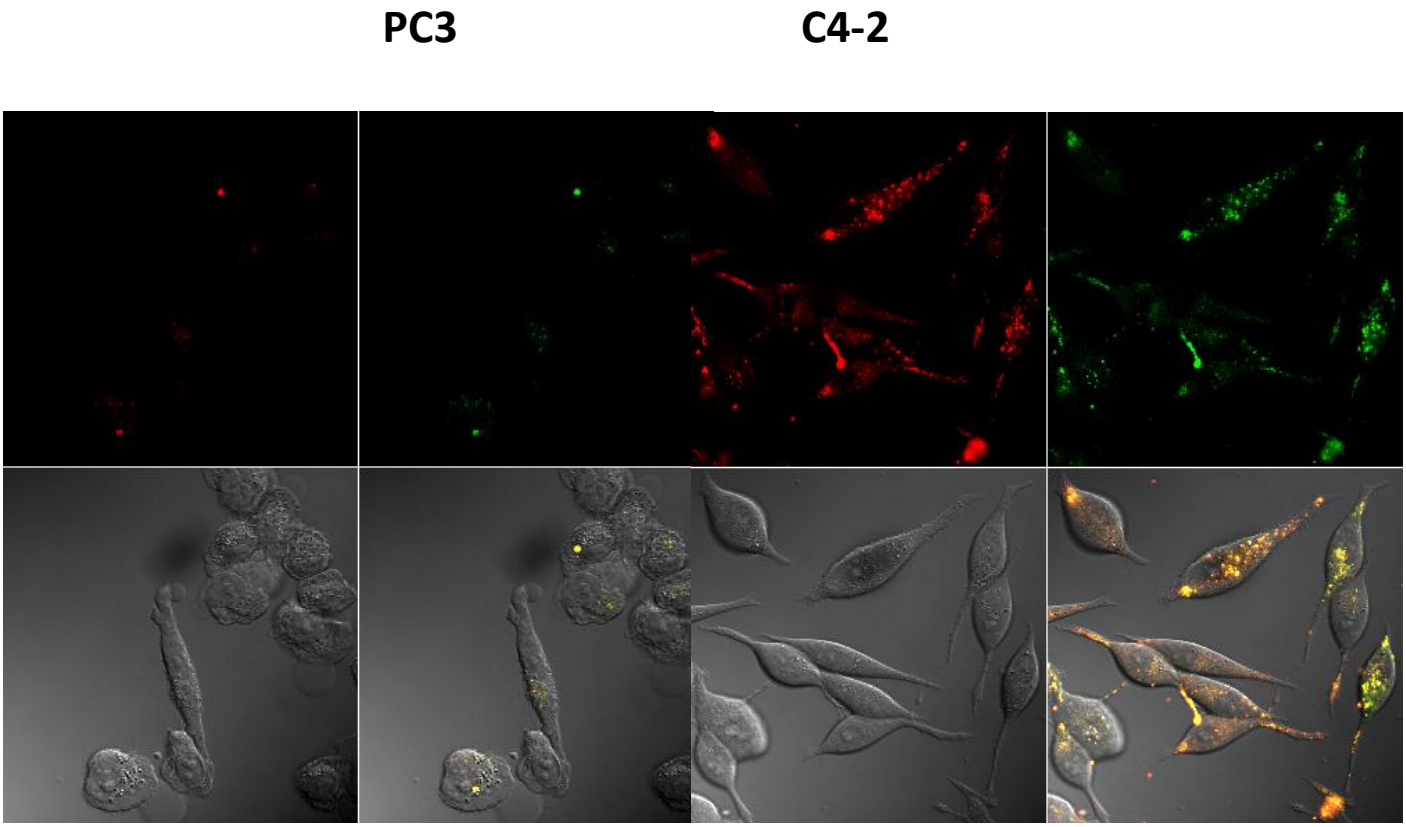

Figure 2. PSMA-specific aptamer dimer specifically binds and becomes internalized by PSMA expressing C4-2 cells. PSMA-null PC3 and C4-2 cells were seeded on chamberglass plates and grown for 2 days at 37°C under 5% CO_2. Old medium was discarded and the cells were incubated for 2 h with 1 μM of PSMA-specific aptamer dimer in RPMI with 10% FBS pre-warmed to 37°C. Cells were then washed with warm fresh RPMI and DPBS followed by a 5 min fixation with 3.7% formaldehyde in DPBS. Cells were visualized under confocal microscope. The dA[16] tailed monomer emits at 670 nm and was shown in red in A and E; while the dT[16] tailed monomer was shown in green in B and F although it emits at 570 nm. Differential interference contrast (DIC) images are shown in C and G, and composite images are shown in D and H.

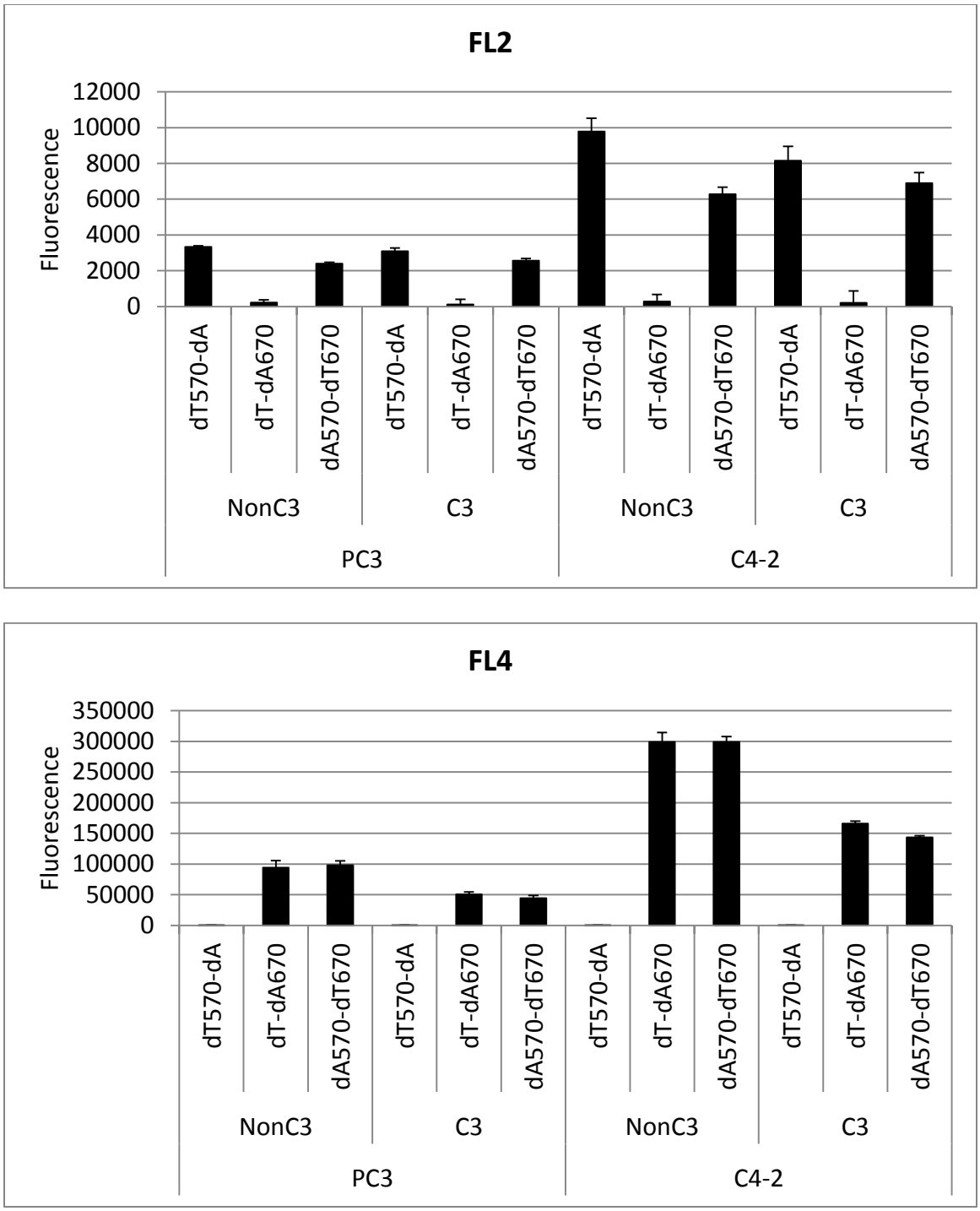

Figure 3. Internalization of PSMA-specific aptamer dimer by PSMA expressing C4-2 cells detected by flow cytometry. PSMA-null PC3 or C4-2 cells were seeded into 24-well cell culture plates and grown for 2 days at 37°C under 5% CO_2. Old medium was discarded and the cells were incubated for 2 hrs with 1 μM of respective PSMA-specific aptamer dimers in RPMI with 10% FBS pre-warmed to 37°C. The cells were then trypsinized, washed with DPBS, and resuspended in DPBS in ice for flow cytometry. FL2 and FL4 channels show the fluorescence at 570 and 670 nm, respectively. Regression analysis shows that C4-2 cells emit significantly higher levels of fluorescence than PC3 ($p < 0.001$).

Our microscopy (Figure 2) and flow cytometry (Figure 3) studies indicate that the $SZTI_{PSMA01}$ DAC has the desired binding characteristics (binding selectively to PSMA+-cells at μM concentrations at room temperature and selective internalization into PSMA+ cells following incubation of μM concentrations at 37 °C. This work is being prepared for publication (appendix #2).

d. Effects of ZnPc complex formation on cellular internalization. The effects of ZnPc complex formation on cellular internalization of monomeric and dimeric aptamer complexes will be evaluated using confocal microscopy and flow cytometry. (Y2: Q1).

Our studies with 24 nucleotide sequence $GCGCA_{16}GCGC$ and corresponding sequence $GCGCT_{16}GCGC$ which can be used to deliver Zn2+ but which we have used to deliver doxorubicin demonstrate that this sequence motif efficiently promotes cellular internalization into PSMA+ prostate cancer cells (Figures 2 & 3; appendix #2).

Aim 2: ***Evaluate the extent to which chelated Zn^{2+} (Zn^{2+}-pyrithione or ZnPc) enhances the cytotoxicity of fluoropyrimidine drugs (FPs) (5FU and FdUMP[10]) towards prostate cancer cells and determine if dimeric aptamer complexes containing both FPs and chelated Zn^{2+} display significantly greater cytotoxicity towards $PSMA^+$ PCa cells than complexes without FPs and/or without Zn^{2+}.*** **(Y1: Q1-4; Y2: Q1-4).**

Task 2.A. Evaluate the cytotoxicity of fluoropyrimidines in combination with Zn2+-chelates towards prostate cancer cells.

a. MTS assays. MTS assays will be used to assess the cytotoxicity of FPs (FdUMP[10] and 5FU) in combination with Zn^{2+}-chelates (Zn^{2+}-pyrithione and ZnPc). (Y1: Q1).

We completed studies demonstrating that FdUMP[10] is highly cytotoxic towards prostate cancer cells and that the cytotoxicity of FdUMP[10] towards prostate cancer cells. Preliminary studies demonstrated that FdUMP[10] cytotoxicity was enhanced by Zn2+-pyrithione. More recent studies indicate the timing of Zn2+ treatment relative to FdUMP[10] treatment is important. If these agents are administered simultaneously, or if Zn2+ is administered before FdUMP[10] there is no benefit to combination treatment (Figure 4).

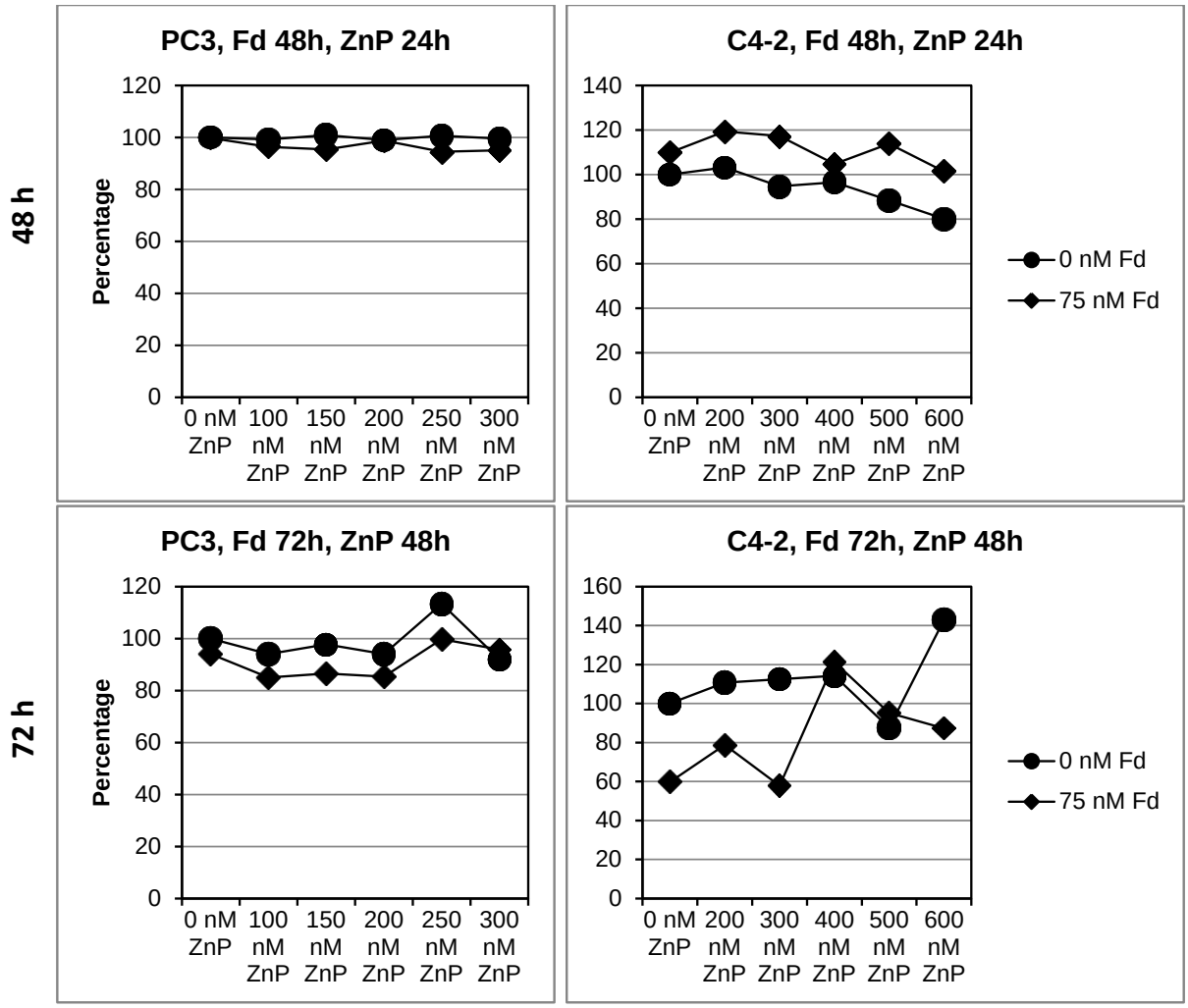

Figure 4. Effects of FdUMP[10] in combination with zinc pyrithione. If the agents are administered simultaneously or if FdUMP[10] is administered first, there is no benefit to combination treatment.

b. Clonogenic assays. Clonogenic assays will be used to assess the effects of FPs and Zn^{2+}-chelates on the clonogenic survival of prostate cancer cells. (Y1:Q2).

We have used a modified clonogenic assay to evaluate the effects of Zn2+ on the cytotoxicity of our novel FdU-containing structures (appendix #1). Although clonogenic assays are useful they are time-consuming and reagent intensive thus our present studies focus on evaluating effects of Zn2+-pyrithione and FdUMP[10] on cell viability and apoptosis using cell-titer glo and caspase glo assays that are fast, reliable, and reasonably priced.

c. Evaluation of synergism. The MTS and clonogenic data will be analyzed using CalcuSyn to determine if the cytotoxicity of FPs and Zn^{2+}-chelates is synergistic, additive, or antagonistic. (Y1; Q3).

We evaluated synergism, however, out studies have demonstrated that the interaction of FdUMP[10] with Zn2+ is more complex than we initially thought. Addition of Zn2+ either prior to FdUMP[10] or simultaneous with FdUMP[10] results in no synergism (Figure 4). There appears to be a positive interaction for very low concentrations of FdUMP1[0] treatment (Figure 5). Interestingly, chelation of Zn2+, especially after FdUMP[10] treatment, appears to be therapeutically beneficial and likely is synergistic (Figure 6).

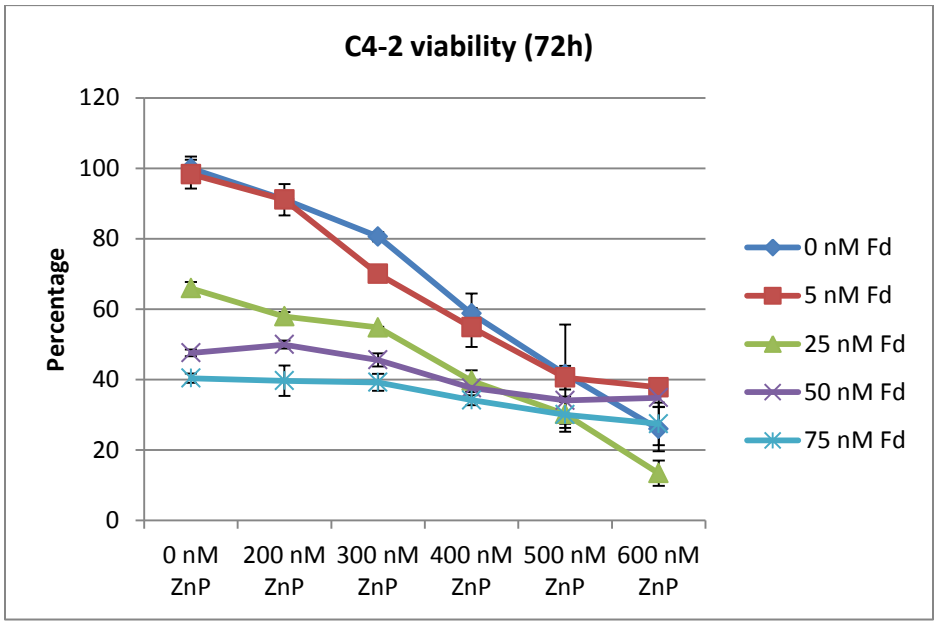

Figure 5. Effects of FdUMP[10] in combination with zinc pyrithione. If the agents are administered simultaneously or if FdUMP[10] is administered first, there is no benefit to combination treatment.

d. Evaluation of apoptotic cell death. A "live/dead" assay will be used to determine the extent of apoptotic cell death induced by FPs, Zn^{2+}-chelates, and the combination of FPs with Zn^{2+}-chelates. Western blots will be used to evaluate caspase and poly(ADP-ribose) polymerase (PARP) cleavage in drug-treated cells. (Y1: Q4).

We have demonstrated that Zn2+-chelation induces apoptosis in prostate cancer cells and are investigating whether Zn2+-chelation after low levels of FdUMP[10] treatment might be an efficient approach for initiating apoptosis in prostate cancer cells. We have been following apoptosis by changes in nuclear morphology consistent with chromatin condensation. Zn2+ chelation with TPEN seems to efficiently induce apoptosis after FdUMP[10] treatment (Figure 6).

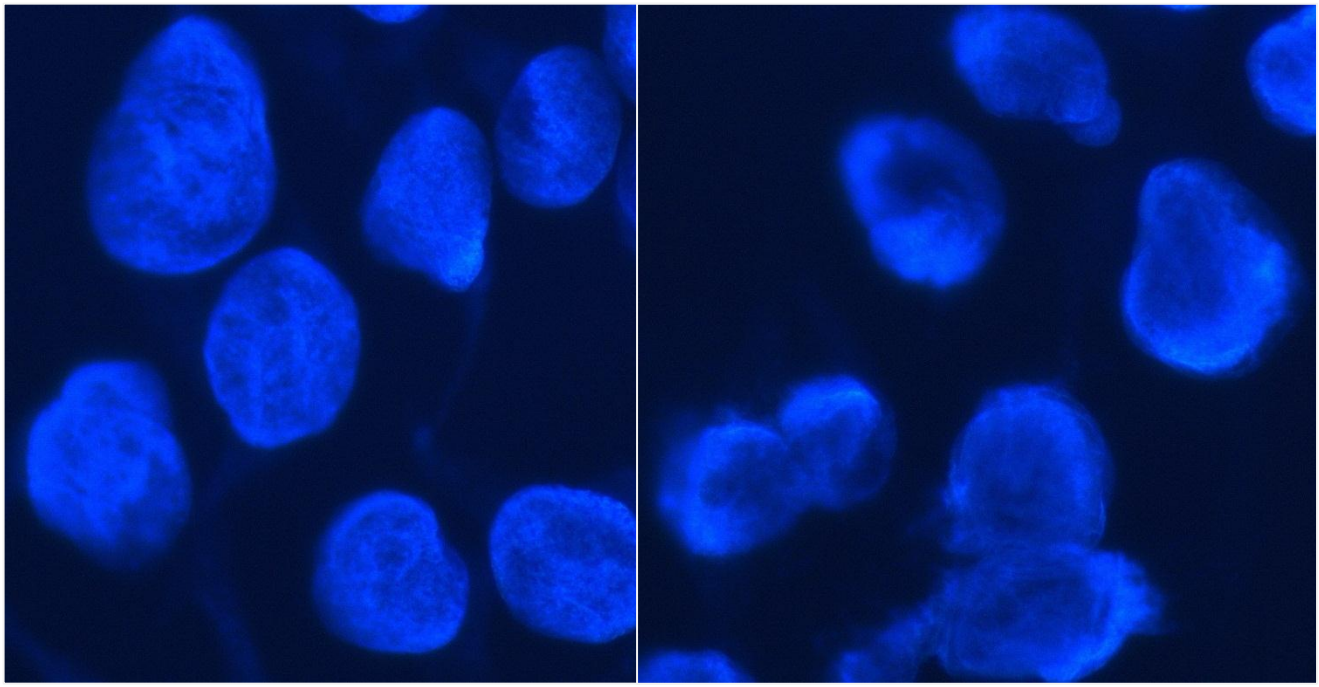

Figure 6. Changes in nuclear morphology after treatment with FdUMP[10] alone for 75 nM for 48 h (left) and the same treatment followed by TPEN for 6 h. Substantial breakdown of nuclear DNA occurs upon TPEN treatment under these conditions.

Task 2.B. Evaluate the selective cytotoxicity of dimeric aptamer complexes containing FdU and/or ZnPc towards PSMA$^+$ prostate cancer cells.

a. Preparation of cytotoxic dimeric aptamer complexes. The dimeric aptamer complex will be prepared with FdU nucleotides by substituting FdU for dT in the dimerization motif. Complexes with ZnPc will be formed by incubation with ZnPc. Control complexes will contain neither FdU nor ZnPc. Specificity of the aptamer will be verified by using a scrambled aptamer sequence. Complex formation will be verified by CD and/or NMR spectroscopy. (Y2: Q1).

We have completed this task using the GCGCA$_{16}$GCGC + GCGCT$_{16}$GCGC sequence motif and demonstrated formation and stability of the dimeric aptamer complex (Figure 1; appendix #2).

b. Specificity of dimeric aptamer complexes for PSMA$^+$ cells. PSMA-transfected and mock-transfected PC3 cells will be used to assess specificity of the dimeric aptamer complex for PSMA$^+$ cells. MTS and/or clonogenic assays will be used to assess cytotoxicity. (Y2: Q2-3).

We have demonstrated that the dimeric aptamer complex is specifically internalized by PSMA+ C4-2 cells relative to PSMA-null PC3 cells using confocal microscopy (Figure 2) and flow cytometry (Figure 3).

c. Induction of apoptosis in PSMA$^+$ cells by dimeric aptamer complexes. Flow cytometry and Western blots will be used to investigate apoptotic cell death following exposure to dimeric aptamer complexes containing FdU and/or ZnPc. (Y2: Q3-4).

We have demonstrated that the dimeric aptamer complex selectively delivers doxorubicin to PSMA+ cells resulting in selective cytotoxicity (Figure 7; appendix #2).

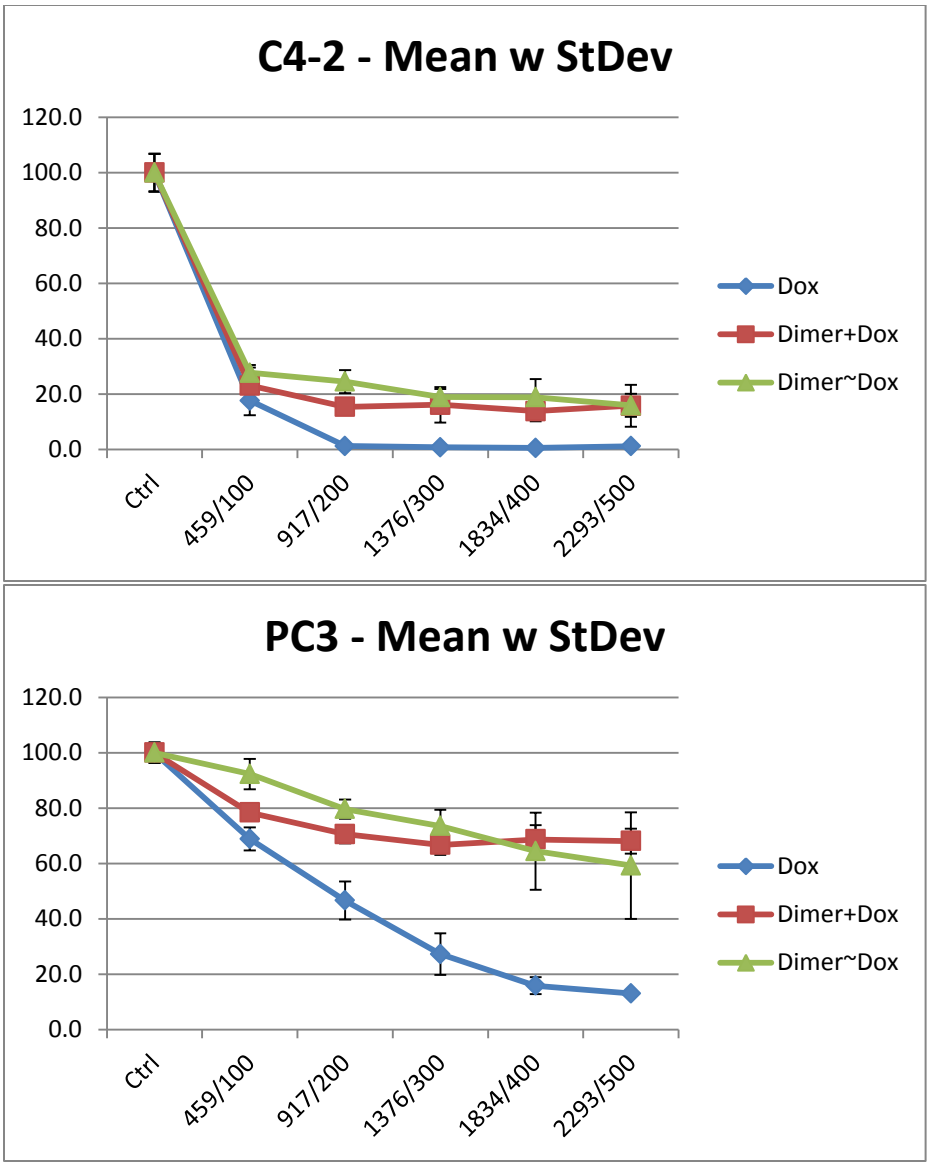

Figure 7. Cytotoxicity of the dimeric aptamer complex with Doxorubicin towards PC3 and C4-2 cells. The dimeric complex displays equivalent cytotoxicity as free doxorubicin towards PSMA+ C4-2 cells but substantially diminished cytotoxzicity towards PSMA-null PC3 cells. The results are consistent with the dimeric aptamer complex selectively delivering doxorubicin to PSMA+ cells.

Aim 3: ***Evaluate the safety and anti-tumor activity of chelated-Zn^{2+} in combination with advanced FPs as well as metallated DNA aptamer complexes that include both chelated Zn^{2+} and FdU.*** (Y2: Q1-4; Y3: Q1-4).

Our experiments with the porphyrin ZnPc binding to DNA resulted in studies with the porphyrin meso-tetra-4-pyridyl porphine (MTP) interacting with single-stranded DNA (ssDNA). We demonstrated formation of discrete nanoparticles (NPs) and went on to show that we could selectively kill bladder cancer cells in a light-dependent manner in vitro and in vivo.

Specifically, we demonstrated that the MTP:DNA NP was safe in vivo (Task 3.A.) and demonstrated the efficacy of the NP towards tumor xenogrfts in vivo (Task 3.B.).

A manuscript summarizing these studies is included in (appendix #4). We are completing studies with an MTP + FdUMP[10] NP as part of our work under the no-cost extension of this project.

KEY RESEARCH ACCOMPLISHMENTS:

- We have created dimeric DNA aptamer constructs that are selectively internalized into PSMA+ cells. This is the first DNA aptamer to PSMA that we are aware of and these are the first studies to show selective targeting of prostate cancer cells with a DNA aptamer (appendix #2).
- We developed a new strategy for covalent attachment of doxorubicin to DNA and demonstrated that this strategy could be used to efficiently kill prostate cancer cells using a DNA hairpin (appendix #3).
- We used the novel chemical conjugation strategy of doxorubicin with our dimeric aptamer constructs and demonstrated a high-lvel of specificity for killing of PSMA+ prostate cancer cells in co-culture experiments with PSMA-null cells.
- We have demonstrated that FdUMP[10] is synergistic with Zn2+ chelators suggesting an alternative approach to Zn2+-delivery for prostate cancer treatment.
- We developed a new nanoparticle (NP) composed of porphyrin and DNA and demonstrated that this NP could be used to kill bladder cancer cells in vitro and to treat bladder cancer xenografts in vivo (appendix #4).

REPORTABLE OUTCOMES:

Ghosh S, Salsbury F, Horita D, Gmeiner, WH. Cooperative Stabilization of Zn2+:DNA Complexes through Netropsin Binding in the Minor Groove of FdU-Substituted DNA J Biomol Struct Dyn 2012. DOI: 10.1080/07391102.2012.732343
http://www.tandfonline.com/doi/abs/10.1080/07391102.2012.732343?url_ver=Z39.88-2003&rfr_id=ori:rid:crossref.org&rfr_dat=cr_pub%3dpubmed&

U.S. Patent Application No. 13/008,614
Cytotoxic Nucleotides for Targeted Therapeutics
Inventor: William H. Gmeiner (Additional office actions completed in 2012 – some allowance of claims is anticipated).

CONCLUSION:

The dimeric aptamer complexes that we developed in this project deliver doxorubicin specifically to prostate cancer cells in a PSMA-dependent manner and these agents have the potential to be highly efficacious and very well-tolerated by patients with advanced prostate cancer. This structural motif can also be used to deliver Zn2+ FdU nucleotides to prostate cancer cells. We believe prostate cancer patients will greatly benefit from these advanced, targeted therapeutic agents. Our studies with the effects of Zn2+ in combination with FdUMP[10] reveal prostate cancer cells are highly sensitive to Zn2+ concentrations with levels higher or lower than optimal resulting in chemosensitization and cell death. These findings enrich our understanding of targeting Zn2+ levels for therapeutic benefit in the treatment of prostate cancer. Our work with porphyrin NPs provides a new approach to treating cancer that our in vivo studies demonstrate is non-toxic and effective for cancer treatment. In summary, we have progressed in all aspects of this project and developed new strategies and key reagents with strong potential for improving treatment of advanced prostate cancer.

REFERENCES:

Ghosh, S., Salsbury, F.R., Horita, D.A., Gmeiner, W.H. Zn2+ selectively stabilizes FdU-substituted DNA through a unique major groove binding motif. **Nucl Acids Res** 2011. PMID: 21296761.

Ghosh S, Salsbury F, Horita D, Gmeiner, WH. Cooperative Stabilization of Zn2+:DNA Complexes through Netropsin Binding in the Minor Groove of FdU-Substituted DNA **J Biomol Struct Dyn 2012**. DOI: 10.1080/07391102.2012.732343
http://www.tandfonline.com/doi/abs/10.1080/07391102.2012.732343?url_ver=Z39.88-2003&rfr_id=ori:rid:crossref.org&rfr_dat=cr_pub%3dpubmed&

APPENDIX:

Appendix #1 (previously reported as submitted)
Published in **J Biomol Struct Dyn** 2012 Nov 16; PMID: 23153072

Cooperative Stabilization of Zn^{2+} :DNA Complexes Through Netropsin Binding in the Minor Groove of FdU-Substituted DNA

Supratim Ghosh[1,2], Freddie R. Salsbury, Jr.[3], David A. Horita[4], William H. Gmeiner[1,2]

[1]Department of Cancer Biology, [2]Program in Molecular Genetics, and [4]Department of Biochemistry, Wake Forest University School of Medicine and [3]Department of Physics, Wake Forest University, Winston-Salem, NC

*Address Correspondence to this author:

Phone (336)716-6216

Fax: (336) 716-0255

bgmeiner@wfubmc.edu

Running Title: Zn^{2+}/Netropsin:DNA cooperative complex formation.

Abstract: The simultaneous binding of netropsin in the minor groove and Zn^{2+} in the major groove of a DNA hairpin that includes 10 consecutive FdU nucleotides at the 3'-terminus (3'FdU) was demonstrated based upon NMR spectroscopy, circular dichroism (CD), and computational modeling studies. The resulting Zn^{2+} /netropsin:3'FdU complex had very high thermal stability with aspects of the complex intact at 85 ^{o}C, conditions that result in complete dissociation of Mg^{2+} complexes. CD and ^{19}F NMR spectroscopy were consistent with Zn^{2+} binding in the major groove of the DNA duplex and utilizing F5 and O4 of consecutive FdU nucleotides as ligands with FdU nucleotides hemi-deprotonated in the complex. Netropsin is bound in the minor groove of the DNA duplex based upon 2D NOESY data demonstrating contacts between AH2 ^{1}H and netropsin ^{1}H resonances. The Zn^{2+}/netropsin:3'FdU complex displayed increased cytotoxicity towards PC3 prostate cancer (PCa) cells relative to the constituent components or separate complexes (e.g. Zn^{2+}:3'FdU) indicating that this new structural motif may be therapeutically useful for PCa treatment.

Introduction

The coordination of metals by nucleic acids has important implications for biology, with metals such as Cd^{2+} and Ni^{2+} imparting toxicity and carcinogenesis(Bal, Schwerdtle & Hartwig 2003; Franzle & Markert 2003; Beyersmann & Hartwig 2008; Hartwig 2010) while metals such as K^{+} and Mg^{2+}(Broxson, Beckett & Tornaletti 2011; Yang & Hayes 2011) play pivotal roles in nucleic acid structure and stability. Zn^{2+} plays a key role in cellular homeostasis in part through its coordination by Zn^{2+}-finger peptidic motifs that are important regulators of protein-protein(Gamsjaeger, Liew, Loughlin, Crossley & Mackay 2007) and protein-nucleic acid(Elrod-Erickson, Rould, Nekludova & Pabo 1996) recognition. An intriguing observation is that Zn^{2+} levels decrease dramatically during prostate cancer (PCa) carcinogenesis with normal prostate characteristically displaying the highest Zn^{2+} levels for any soft tissue in the human body(Kelleher, McCormick, Velasquez & Lopez 2011) while PCa displays low levels of Zn^{2+}.(Christudoss, Selvakumar, Fleming & Gopalakrishnan) Exogenous Zn^{2+} is cytotoxic towards PCa cells and Zn^{2+}-treatment sensitizes PCa cells to chemotherapy.(Uzzo et al. 2002)

5-Fluoro-2'-deoxyuridine (FdU) is a non-native thymidine analog that has anti-cancer activity as a consequence of metabolism to the thymidylate synthase (TS) inhibitory metabolite FdUMP (Gmeiner 2005) and the incorporation of the nucleotide triphosphate FdUTP into DNA that results in poisoning of DNA Topoisomerase 1.(Liao et al. 2005; Gmeiner W.H. 2010; Gmeiner, Salsbury, Olsen & Marky 2011; Pardee, Gomes, Jennings-Gee, Caudell & Gmeiner 2012) FdU is readily cleaved by glycosidase activities *in vivo* to 5FU and 5FU is widely used to treat diverse malignancies imparting a significant survival advantage for treatment of colorectal cancer. 5FU is inefficiently converted to FdUMP and FdUTP, however, and thus there is a need for alternative approaches to deliver DNA-directed fluoropyrimidine (FP) drugs. Our laboratory has pioneered the use of DNA polymers of FdUMP with FdUMP[10] showing particularly strong cytotoxicity and a unique spectrum of activity in the NCI 60 cell line screen.(Gmeiner W.H. 2010)

The chemosensitization of PCa cells by Zn^{2+} raises the possibility that Zn^{2+} chelates of FdU-oligodeoxynucleotides might be useful for treating advanced PCa. Zn^{2+} was reported to form specific complexes with FdU-substituted DNA(Lee, Latimer & Reid 1993) and coordination of Zn^{2+} by deprotonated FdU was proposed as the basis for specific complex formation. Zn^{2+}-DNA complexes

formed under similar conditions were however, found to be the result of inter-strand aggregation.(Spring & Clegg 2007) We recently reported that Zn^{2+} formed specific complexes with FdU-substituted DNA hairpins provided the DNA sequence contained several consecutive FdU nucleotides.(Ghosh, Salsbury, Horita & Gmeiner 2011) Biophysical characterization and computational chemistry approaches revealed Zn^{2+} bound FdU-substituted DNA in the major groove. Zn^{2+} was bound in a trigonal bipyramidal geometry with F5 from one FdU and O4 from an adjacent FdU serving as axial ligands for Zn^{2+} coordination. Zn^{2+} complexation required hemi-deprotonation of FdU nucleotides with F5 being activated for coordination by deprotonation. Hemi-deprotonation of the complex occurs near physiological pH consistent with the pK_A for FdU (~7.6).

The occupancy of the major groove of DNA through Zn^{2+} complexation raises the possibility that Zn^{2+}:DNA complexes could be further stabilized by binding of ligands in the minor groove. Minor groove binding may impart greater thermodynamic stability to the Zn^{2+}:DNA complex and could potentially result in increased uptake into tumor cells through reduced charge density since minor groove binding ligands(Nelson, Ferguson & Denny 2007), such as netropsin(Lewis et al. 2011), carry positive charges that partially offset the highly negative charge of the phosphodiester backbone of DNA. In this work, we demonstrate that

netropsin and Zn^{2+} simultaneously occupy the minor and major groove in the DNA hairpin 3'FdU that includes 10 consecutive FdU nucleotides at the 3'-terminus (**Fig. 1**). CD and NMR spectroscopy indicate the binding of Zn^{2+} occurs via a similar structural motif as occurs for the Zn^{2+}:DNA complex while 2D NMR spectroscopy verifies that netropsin binds in the minor groove formed from A-FdU base pairs similar to the binding motif established for A-T base pairs. The resulting Zn^{2+}/netropsin:3'FdU complex is highly cytotoxic towards PCa cells consistent with this unique structural motif being useful for PCa treatment.

Methods

Formation of Zn^{2+}:DNA Complexes: Intramolecular hairpins were formed using 1 mM DNA in dH_2O by heating to 80°C for 5 min followed by rapid cooling. Native gel electrophoresis described in the previous studies confirmed intramolecular DNA hairpin formation(Ghosh et al. 2011). Zn^{2+}/netropsin:3'FdU (or Mg^{2+}) complexes were formed by incubating 100 μM DNA with 0 – 250 μM netropsin and 0 to 5 mM $ZnCl_2$ (or $MgCl_2$) in M-DNA buffer (20 mM sodium cacodylate, pH 8.0, 10 mM NaCl) for 1 hour at room temperature. The formation of specific Zn^{2+}/netropsin:3'FdU trimolecular complexes was evaluated using an EtBr exclusion fluorescence assay as previously described.(Ghosh et al. 2011) This assay was performed by combining 20 μL of the above described trimolecular complex with 80

μL of EtBr solution (10 mM NaCl, 20 mM sodium cacodylate, pH 8.0, + 25 μM EtBr) followed by incubation for 30 min at room temperature in a 96-well clear bottom, black plate (Costar). The final 3'FdU concentration was 20 μM and divalent metal and netropsin concentration ranged from 0 to 1 mM and 0 to 50 μM respectively. EtBr fluorescence was detected using a Typhoon-9210 variable mode imager with Green laser (532nm) excitation and 610 nm emission filter (with 500 PMT set). Fluorescence intensity was quantified with the software ImageQuant5.2 and graphed vs netropsin concentration.

Analytical Characterization of DNA:Zn^{2+} Complexes. Zn^{2+}/netropsin:3'FdU and Mg^{2+}/netropsin:3'FdU trimolecular complexes were analyzed by circular dichroism (CD) and NMR spectroscopy to characterize their structural features and any specific changes induced by netropsin and Zn^{2+} (or Mg^{2+}). 300 μL of 20 μM solution of DNA with 0, 25, 50μM netropsin and 0, 0.5mM Zn^{2+} (or Mg^{2+}) were prepared in M-DNA buffer as described above and used to obtain the CD spectrum. An Aviv CD spectrometer was used to scan the region from 210 – 350 nm at a rate of 0.5 nm/sec. Temperature was controlled at 20 ^{o}C. For temperature-dependent CD studies, temperature was increased from room temperature to 37, 55, 70, 85 ^{o}C respectively and allowed to equilibrate for an additional minute then spectra were acquired at the above mentioned temperature.

^{1}H, ^{19}F, and ^{31}P NMR spectroscopy were used to investigate specific structural perturbations induced by netropsin and Zn^{2+} to the 3'-FdU hairpin. For the NMR analysis, 500 μL of 0.5 mM 3'FdU in M-DNA buffer modified to contain 50 mM sodium cacodylate were used. NMR samples contained 0.5mM netropsin and either no metal, 5mM Zn^{2+} or 5 mM Mg^{2+}. 10% D_2O was included to maintain lock. The final pH of the samples was adjusted to 8 (+/- 0.1 pH unit).

^{1}H NMR spectra were collected using a Bruker Avance DRX 600 MHz spectrometer with a TXI Cryoprobe at room temperature using the WATERGATE sequence with a 3-9-19 refocusing pulse. Nulls were set at +/- 18.1 ppm. Spectra were acquired with a spectral width of 33.3 ppm, 8192 total data points, and 256 scans. Two-dimensional NOESY experiments were acquired at 25 °C using a 3 s relaxation delay, a 200 ms mixing time, 48 scans per increment, 4096 x 256 complex points, and 3-9-19 WATERGATE solvent suppression (Sklenar, Piotto, Leppik & Saudek 1993). Data were processed using NMRPipe (Delaglio et al. 1995).

^{19}F and ^{31}P NMR spectra were acquired using a Bruker 300 MHz NMR instrument with QNP probe at room temperature using inverse gated proton decoupling. In case of ^{19}F spectra were acquired with a spectral with of 100 ppm, 7000 total data

points and 1000 scans. ^{31}P spectra were acquired with a spectral with of 400 ppm, 65536 total data points and 1000 scans. Both ^{19}F and ^{31}P spectra were acquired with concentric internal standard capillaries (Wilmad) 85% H_3PO_4 (δ = 0 ppm) or 5mM aqueous solution of KF (δ =125.3ppm). NMR spectra were processed with Mestrec 4.995 software and referenced to internal standards.

T_m analysis: Temperature-dependent melting (T_m) of the 3'FdU DNA hairpin complexed or not complexed with Zn^{2+} /Mg^{2+} and/or netropsin was determined using UV absorption spectroscopy at 260 nm. 400 μL of a 2.5 μM solution of the annealed hairpins in M-DNA buffer in the presence of 5μM netropsin and 0.5 mM Zn^{2+} (or Mg^{2+}) were analyzed using a Beckman Coulter DU-800 UV-Vis spectrophotometer in the temperature region 20 – 85 ^{o}C. Temperature was increased at a rate of 0.5 ^{o}C/min. Melting temperatures were estimated from the percent increase in hyperchromicity.

Cytotoxicity of FdU Hairpins and Zn^{2+} Complexes. The cytotoxicity of the 3'FdU-netropsin-Zn^{2+} trimolecular complexes was determined using a modified clonogenic assay with an MTT read-out. PC3 prostate cancer cells were seeded in 24 well plates at a cell density of 1000 cells/well with 500 μL complete media (RPMI + 10%FBS + 1% Penicillin & Streptomycin (pen/strep)). After 24 hours,

media was removed and cells were washed twice with 500 μL PBS followed by addition of 500 μL serum and pen-strep free RPMI (pH-8.0). The 3'FdU-netropsin-Zn^{2+} complex was formed by incubating 10 μM 3'FdU hairpin with 0.2 mM netropsin and 0.5 mM Zn^{2+} in serum- and antibiotic-free RPMI (pH-8.0) at room temperature for 1 hour. The cells were then treated with the above complex and incubated at 37 ^{o}C in a CO_2 incubator. After 24 hours, media was replaced with fresh, complete media and incubated at 37,^{o}C for a total of 14 days with media changes every 2 days. Cell viability was then assessed using an MTS assay. Wells were washed with sterile PBS followed by addition of 250,μL fresh complete media. Then 25μL CellTiter 96 AQ_{ueous} One Solution Cell Proliferation Assay reagent (Promega) was added to each well and incubated at 37 ^{o}C for 3 hours in a CO_2 incubator. 200μL of the resultant solution from each well were transferred to a transparent 96-well plate and the absorbance was measured at 490nm using Spectra Max-340PC microplate reader. All experiments were done in triplicate. Each set of data (net absorbance) were then expressed as a percentage, considering the no treatment group as 100%.

Computational Modeling. The initial models for the Zn^{2+} complexes were derived from coordinates for six consecutive base pairs and netropsin extracted from the NMR solution structure (pdb 1Z8V) (Van Hecke, Nam, Nguyen & Van Meervelt 2005). Conversion to A-FdU was performed by first rebuilding the A-T

DNA chain using the coordinate building tools within CHARMM (Brooks et al. 2009) on the original pdb backbone, and the deleting the thymidine methyl group and replacement with fluorine. In keeping with our previous work (Ghosh et al. 2011), every other FdU base nitrogen was deprotonated to form the hemi-protonated states. Also based on our previous work, (Ghosh et al. 2011) Zn^{2+} complexes with three water molecules were added to the DNA/netropsin complex. This was attempted with six, three and two complexes spaced evenly, however, only the two Zn^{2+}/three water complexes formed stable complexes with netropsin/DNA. Geometry optimizations were performed on the entire complex, with Mg^{2+} counterions added in the vicinity of the backbone phosphorus. The structures were geometry-optimized with Gaussian 03 using PM3 in Cartesian coordinates (Ghosh et al. 2011). Post-optimization, single-point calculations were performed with a minimal basis set (STO-3g*) for an Natural Bond Orbital analysis (Frisch 2004) from which the Wieburg bond orders were extracted.

RESULTS

Stabilization of Zn^{2+}:DNA Complexes through Netropsin Binding: We have previously established that DNA sequences consisting, in part, of consecutive dA-FdU base pairs, such as the DNA hairpin sequence 3'FdU (**Fig. 1**) form highly

stable complexes with Zn^{2+}. Zn^{2+} complex formation occurs via major groove binding to the DNA duplex and requires hemi-deprotonation of the FdU imino hydrogens. As netropsin is known to bind in the minor groove of duplex DNA selectively at runs of consecutive dA-dT base pairs, we sought to determine if netropsin would also bind to consecutive dA-FdU base pairs and, if so, to determine to what extent netropsin binding (likely in the minor groove) would cooperatively stabilize Zn^{2+}-binding in the major groove of the 3'-FdU sequence. The minor groove atomic configuration for FdU-substituted DNA sequences, such as the 3'FdU DNA hairpin, is identical to that for DNA sequences consisting of dA-dT base pairs making it likely that netropsin would bind in a similar manner. Further, netropsin binding would be expected to reduce base pair dynamics for DNA complexes.(Zimmer, Puschendorf, Grunicke, Chandra & Venner 1971) This reduced flexibility could result in cooperative enhancement of Zn^{2+}-binding in the major groove if the preferred geometries for DNA in the netropsin complex and the Zn^{2+} complex were similar.

The propensity for netropsin binding to alter the formation and stability of Zn^{2+} complexes with the hairpin 3'FdU were studied using EtBr exclusion assays (**Fig. 1c,d** and **Supplementary Fig. 1**) and UV (**Supplementary Fig. S2**) and CD (**Fig. 2**) thermal melting studies. We have previously shown that EtBr intercalation into

3'FdU is inhibited by Zn^{2+} complexation (Ghosh et al. 2011), but is not blocked by Mg^{2+} binding. Netropsin binding alone inhibited EtBr intercalation consistent with netropsin binding 3'FdU and stabilizing the duplex in a manner that prevents EtBr intercalation. Consistent with our previous results, Zn^{2+}-binding alone inhibited EtBr intercalation. Interestingly, the combination of Zn^{2+} and netropsin was more effective at inhibiting EtBr intercalation than either agent alone, consistent with cooperativity in the binding of these moieties to distinct sites on the DNA duplex (**Fig. 1c,d**).

The thermal stability of the 3'FdU complex with Zn^{2+} and netropsin (Zn^{2+}/netropsin:3'FdU) was further investigated using UV hyperchromicity (**Supplementary Fig. S2**) and temperature-dependent CD spectroscopy (**Fig. 2**). We had previously demonstrated that Zn^{2+} complexation resulted in a substantial increase in thermal stability for 3'FdU while Mg^{2+} binding had a more moderate stabilizing effect.(Ghosh et al. 2011) UV hyperchromicity measurements revealed that the sigmoidal-shaped curve typically observed in such experiments did not occur for Zn^{2+}/netropsin:3'FdU although such sigmoidal curves were detected for the Mg^{2+}/netropsin:3'FdU complex and the netropsin:FdU complex (**Supplementary Fig. 2**). The overall increase in absorbance (260 nm) for both the Mg^{2+}/netropsin:3'FdU complex and the netropsin:3'FdU complex was the 20-25%

that is typical for melting duplex DNA and both complexes had similar T_m values. In contrast, Zn^{2+}/netropsin:3'FdU displayed a maximum increased absorbance of about 15% indicating strand-dissociation was not complete, even at temperatures above 80 °C. These results indicate that Zn^{2+} and netropsin may cooperatively stabilize 3'FdU and that the Zn^{2+}/netropsin:3'FdU complex likely undergoes step-wise dissociation with the complex remaining incompletely dissociated even at elevated temperatures.

CD Spectral Analysis: The structure and stability of Zn^{2+}/netropsin:3'FdU was further evaluated by CD spectral analysis, including temperature-dependent studies, to determine to what extent Zn^{2+} and netropsin binding, both singly and in combination, alters DNA structure and to gain further insight into the thermal stability of the complex (**Fig. 2**). Our previous studies demonstrated that Zn^{2+}, but not Mg^{2+}, induced a concentration-dependent blue-shift of approximately 20 nm for the maximal positive ellipticity (280 -> 260 nm) for 3'FdU.(Ghosh et al. 2011) The effects of netropsin binding to 3'FdU are similar to that observed previously for binding to A-T rich DNA duplex sequences and involve a slight red-shift for the maximal positive ellipticity (280 -> 285 nm), a sharp new maximum at 260 nm, and a broad new maximum at approximately 320 nm (**Fig. 2**). The red-shift for the maximal ellipticity and the new maxima at 260 nm likely involve slight structural

alterations for the A-FdU base pairs to accommodate netropsin binding in the minor groove while the new 320 nm maxima reflect the binding of N-methyl pyrrole moieties of netropsin in the minor groove of 3'FdU.(Zimmer, Marck, Schneider & Guschlbauer 1979)

CD spectra for 3'FdU:netropsin revealed highly specific alterations to the structure and stability of the complex were induced by Zn^{2+} (**Fig. 2a,c**), but not Mg^{2+} (**Fig. 2b,d**). Mg^{2+} induced moderate attenuation of the maxima at 260, 280, and 320 nm with minimal shifts in the maxima location. In contrast, Zn^{2+} substantially enhanced the maxima at 260 nm (~4-fold increase relative to netropsin:3'FdU) and a marked reduction in the maxima at 320 nm. The enhancement for the 260 nm maxima likely reflects Zn^{2+}-induced structural perturbations to the FdU nucleobases that are re-enforced by netropsin binding. The thermal stability of 3'FdU complexes with netropsin and/or Zn^{2+} (or Mg^{2+}) were further investigated by temperature-dependent CD spectroscopy. The maxima at 260, 280, and 320 nm were reduced by approximately 50% upon increasing the temperature from 37 to 70 °C. Further temperature increase to 85 °C resulted in near complete loss for these maxima. The temperature sensitivity for CD spectra of the Mg^{2+}/3'FdU complex were nearly indistinguishable from netropsin:3'FdU indicating Mg^{2+} had little effect on the thermal stability of this complex. In contrast, the 260 nm

maxima for the Zn^{2+}/netropsin:3'FdU complex was attenuated by only ~10% upon increasing the temperature from 37 to 70 °C and the intensity for this maxima was reduced only about 30% upon increasing the temperature to 85 °C. These results are consistent with Zn^{2+} and netropsin binding cooperatively to 3'FdU and resulting in formation of a highly stabilized complex.

NMR Spectroscopy: The interactions of Zn^{2+} and netropsin with 3'FdU in the context of the Zn^{2+}/netropsin:3'FdU complex were investigated using NMR spectroscopy. Our previous studies with the Zn^{2+}/3'FdU complex revealed significant downfield shifts for approximately one-half of the ^{19}F resonances relative to 3'FdU in the absence of Zn^{2+}.(Ghosh et al. 2011) Computational and modeling studies indicated that F served as one ligand for Zn^{2+} coordination in the Zn^{2+}/3'FdU complex and that F was activated through deprotonation of the FdU imino ^{1}H which occurred for about one-half of FdU nucleotides under the experimental conditions used. ^{19}F NMR spectra for Zn^{2+}/netropsin:3'FdU revealed similar ^{19}F downfield shifts occurred for this complex consistent with Zn^{2+} coordination involving F in this complex, as well (**Supplementary Fig. 3a**). In contrast, no significant changes were noted in the ^{19}F NMR spectrum for the Mg^{2+}/netropsin:3'FdU complex and netropsin alone did not induce such changes to the ^{19}F spectrum (**Supplementary Fig. 3a**). ^{31}P NMR spectra indicated no

significant change upon Zn^{2+} and/or netropsin binding to 3'FdU although changes were detected for Mg^{2+}/netropsin consistent with Mg^{2+}, but not Zn^{2+}, interacting with the phosphodiester backbone of 3'FdU (**Supplementary Fig. 3b**).

The interactions of Zn^{2+} and netropsin with 3'FdU were further analyzed by 1D and 2D ^{1}H NMR spectroscopy. Imino ^{1}H resonances for FdU nucleotides were readily detected at characteristic frequencies for the Zn^{2+}/netropsin:3'FdU complex consistent with our previous studies(Ghosh et al. 2011) indicating hemi-deprotonation, rather than full deprotonation, was required for complex formation (**Supplementary Fig. 3c**). 2D NOESY spectra were obtained to gain insight into the binding of netropsin to 3'FdU (**Fig. 3** and **Supplementary Fig. 4**). The binding of netropsin, or other putative minor groove binding ligands, at A-FdU (rather than A-T) base pairs had not been described previously, however our 2D NOESY studies demonstrate netropsin interacts with 3'FdU in the minor groove. NOESY crosspeaks were observed between resonances with chemical shifts consistent with an AH2 resonance assignment and those consistent with the pyrrole ^{1}H resonances of netropsin (**Fig. 3**). NOESY crosspeaks from FdU imino ^{1}H to putative AH2 resonances were not detected, however, preventing unambiguous assignment of the AH2 resonances. The lack of imino ^{1}H – AH2 resonances likely resulted from reduced intensity for FdU imino ^{1}H as a consequence of hemi-

deprotonation of FdU in the Zn^{2+} /netropsin:3'FdU complex. Interestingly two AH2-AH2 crosspeaks were present for the netropsin:3'FdU complex that were not observed for 3'FdU consistent with increased π–π stacking for A residues in the context of netropsin:3'FdU complex (**Supplementary Fig. 5**).

Cytotoxicity of Zn^{2+}/netropsin:3'FdU to PC3 Cells. Our previous studies demonstrated that 3'FdU is cytotoxic to PC3 prostate cancer cells and that Zn^{2+} complexation increased the cytotoxic effects (Ghosh et al. 2011). In these studies, the Zn^{2+}/3'FdU complex was delivered to cells using oligofectamine both to enhance cellular permeability and because the complex was labile under conditions used in the tissue-culture experiments. In light of the increased thermal stability for Zn^{2+}/netropsin:3'FdU relative to the Zn^{2+}/3'FdU complex we sought to determine if this complex might display increased cytotoxicity towards PCa cells. Cytotoxicity was determined using a modified clonogenic assay with an MTS assay readout.(Ghosh et al. 2011) Under the conditions used for these experiments the 3'FdU hairpin and the Zn^{2+}/3'FdU complex displayed similar cytotoxicity consistent with dissociation of Zn^{2+} which had moderate cytotoxicity as a single agent (**Fig. 4**). The netropsin:3'FdU complex displayed slightly lower cytotoxicity than 3'FdU, and netropsin as a single agent actually increased viability relative to control cells. These results indicate netropsin is growth-stimulatory towards PCa cells, a surprising finding in light of the antitumor/antibiotic activity described

previously for netropsin.(Soderlind et al. 1999) The Zn^{2+}/netropsin:3'FdU complex displayed enhanced cytotoxic effects relative to the individual components (Zn^{2+}, netropsin, 3'-FdU) and relative to Zn^{2+}/3'FdU complex. In light of the proliferative effects of netropsin, these findings demonstrate that netropsin is likely enhancing the cytotoxicity of the Zn^{2+}/netropsin:3'FdU complex by stabilizing the complex and possibly through enhanced cellular uptake.

Computational Modeling of Zn^{2+}/netropsin:3'FdU. The preferred geometry for Zn^{2+} binding to DNA sequences containing six FdU nucleotides with netropsin was calculated using Gaussian 03.(Frisch 2004) Specifically, the coordinates for six consecutive base pairs were extracted from the structure for a DNA bound to netropsin (rcsb ID; 178V(Van Hecke et al. 2005)). The DNA chain was truncated to include just six base pairs along netropsin and computationally mutated with the sequence and building tools in CHARMM(Brooks et al. 2009) to an A-FdU sequence, but with the backbone provided from the original pdb file.

The geometry and charge distribution for the complex were optimized in an approximation to the 'biological pH state' in which every other FdU was ionized. Zn^{2+} complexes with three water molecules were added to the system in geometries mimicking that of our previous study. Two, three, and six Zn^{2+} complexes were

added for different calculations, but only a two Zn^{2+} system was found to stably bind. The overall geometry and charge distribution were optimized for minimal energy as described in the methods. The structure of each binding site with the Zn^{2+} interacting with adjacent nucleotide bases is shown in **Fig. 5**. As expected from our previous study(Ghosh et al. 2011), in each site the Zn^{2+} is located in the major groove with simultaneous interactions with the O4 carbonyl oxygen of the 3'-terminal FdU and F5 of the 5'terminal FdU, which is deprotonated in the low energy structure. However, in site 2, the Zn^{2+} also interacts with the O4 of the 5' FdU.

More specifically, in site one, the Zn^{2+} is coordinated by three water molecules with an average distance of 2.13 Å to the oxygen atoms in the water molecules and with an average bond order of 0.314 (**Supplementary Table 1**). In site one, the Zn^{2+} is also coordinated by the above-mentioned F with a distance of 3.19 Å, a bond order of 0.006, and is coordinated by the previously mentioned O4 with a distance of 1.9 Å with a partial covalent bond (bond order 0.525 – **Supplementary Table 1**). This coordination is similar to that in our dinucleotide model where the Zn^{2+} had four electrostatic interactions with three water molecules and an F5, and a partial covalent bond with O4. (**Supplementary Table 1**). The interaction with

the Zn^{2+} is more covalent, but the general mode of interaction is robust between the two models.

In the second site, much of the coordination is preserved, however, there is a key difference in the interaction with the 5'-nucleotide; rather than just an electrostatic interaction with the F5, there is also a close, partially covalent interaction with the O4 of that nucleotide. While there are still three water molecules coordinating the second Zn^{2+}, with an average O-Zn^{2+} distance of 2.1 Å and an average bond order of 0.273, and the F5 interactions is still predominately electrostatic (3.03 Å with a bond order of 0.0186), the interactions with the O4 atoms are different for this site. There are two partial covalent bonds to the two different O4 atoms with bond orders of 0.32, and 0.5619. The lower bond order corresponds to the short distance, 1.92 Å, whereas the other O4 is further away at 2.01 Å. These findings indicate that there is a combination of electrostatic and covalent bonding with the O4 of each of the two flanking nucleotides with the Zn^{2+} in the second binding site.

Discussion:

The present work demonstrates that Zn^{2+} and netropsin can simultaneously bind DNA hairpin sequences containing consecutive FdU nucleotides with Zn^{2+} occupying the major groove and netropsin binding the minor groove of the DNA

double helix. The evidence in support of this unique structural configuration includes CD spectral data which are consistent with perturbations to the DNA nucleobases occurring in a Zn^{2+}- and netropsin-dependent manner. The NMR spectral data also were consistent with the major groove binding motif for Zn^{2+} previously established based on NMR and computational chemistry data from our laboratory and with netropsin binding in the minor groove based upon NOE data from pyrrole ^{1}H of netropsin and AH2 ^{1}H resonances in the minor groove of the 3'-FdU hairpin.

The simultaneous binding of netropsin and Zn^{2+} to 3'-FdU resulted in significant stabilization of the complex. The thermal stability of the Zn^{2+}/netropsin:3'FdU complex could not be completely assessed by UV hyperchromicity measurements because complete strand dissociation was not achieved, even for the highest temperatures used for these studies (~85 ^{o}C). Temperature-dependent CD data demonstrated that the complex remained largely intact at 70 ^{o}C and remained at least partially present at 85 °C. This high thermal stability was found to correlate with improved cytotoxicity consistent with the complex persisting under physiological conditions for times sufficient for cellular uptake. The improved stability for the Zn^{2+}/netropsin:3'FdU may be useful for *in vivo* studies and result in increased circulation times for the intact complex relative to linear

homopolymers of FdUMP, such as FdUMP[10] which has shown promise in pre-clinical studies for cancer treatment.(Pardee et al. 2012)

The ability to simultaneously target the major and minor grooves of DNA with potentially cytotoxic moieties as well as to incorporate cytotoxic nucleotides into DNA provides an opportunity to create moderately-sized multi-modality DNA therapeutic complexes that are based on non-covalent chemistry. The present studies have demonstrated proof of principle using netropsin as the minor groove binding ligand with Zn^{2+} occupying the major groove. Somewhat surprisingly, netropsin alone was somewhat growth stimulatory to PCa cells in these studies however the approach demonstrated here is applicable to other minor groove binding drugs, of which there are many, several of which are likely to enhance the anti-tumor activity of 3'FdU when delivered as non-covalent complexes. As our studies with the linear homopolymer, FdUMP[10] indicate that DNA delivery of cytotoxic nucleotides is likely to impact treatment of cancer, the approach demonstrated here using non-covalent chemistry to create multi-modality DNA complexes may also be very useful for cancer treatment.

The structural basis for the high thermal stability of the Zn^{2+}/netropsin:3'FdU complex appears to arise from cooperative binding. Both netropsin-only and Zn^{2+}-

only binding to 3'-FdU induce a new maxima at 260 nm in CD spectra, likely as a result of perturbations in the structure of the FdU nucleobases. This maxima is significantly enhanced upon simultaneous binding of Zn^{2+} and netropsin consistent with cooperativity among the two types of binding. The NMR spectral data indicate that Zn^{2+} complexation for Zn^{2+}/netropsin:3'FdU occurs in a manner similar to that observed previously for the Zn^{2+}/3'FdU complex. While computational studies support a similar binding mode for Zn^{2+} as described previously, they clarify the overall stoichiometry of Zn^{2+} binding (2 Zn^{2+} are bound per 6 FdU nucleotides) and also identify a second binding mode that represents a slight perturbation from the original binding motif. In this second binding mode both O4 and F5 from the deprotonated FdU form partial covalent bonds with Zn^{2+}. Both 2D NMR and computational modeling studies indicate netropsin binds 3'-FdU in the minor groove with similar interactions as have been described previously with A.T-rich DNA sequences.

In summary, we have prepared a unique non-covalent complex that includes DNA with incorporated cytotoxic nucleotides, a minor groove binding ligand with potential anti-tumor activity, and Zn^{2+}, a divalent metal that is cytotoxic to advanced PCa cells. The efficient use of both the minor and major groove of DNA enhances the cytotoxic potential of these complexes. The resulting complexes

have very high thermal stability and display enhanced cytotoxicity towards PCa cells.

Acknowledgements

This work was supported by DOD PCRP 093606 (WHG), National Institutes of Health CA102532 (WHG), 2P30 CA12197-25, and the North Carolina Biotechnology Center. FRS acknowledges partial support from NIH CA12937. All calculations were performed on the DEAC cluster which is supported by WFUS Information systems and the WFU Provost's office. The authors acknowledge Dr. Marcus Wright for help with acquisition of ^{31}P and ^{19}F NMR.

References

Bal, W., Schwerdtle, T. & Hartwig, A. (2003). Mechanism of nickel assault on the zinc finger of DNA repair protein XPA. *Chem Res Toxicol 16*: 242-248.

Beyersmann, D. & Hartwig, A. (2008). Carcinogenic metal compounds: recent insight into molecular and cellular mechanisms. *Arch Toxicol 82*: 493-512.

Brooks, B. R., Brooks, C. L., 3rd, Mackerell, A. D., Jr., Nilsson, L., Petrella, R. J., Roux, B., Won, Y., Archontis, G., Bartels, C., Boresch, S., Caflisch, A., Caves, L., Cui, Q., Dinner, A. R., Feig, M., Fischer, S., Gao, J., Hodoscek, M., Im, W., Kuczera, K., Lazaridis, T., Ma, J., Ovchinnikov, V., Paci, E., Pastor, R. W., Post, C. B., Pu, J. Z., Schaefer, M., Tidor, B., Venable, R. M., Woodcock, H. L., Wu, X., Yang, W., York, D. M. & Karplus, M. (2009). CHARMM: the biomolecular simulation program. *J Comput Chem 30*: 1545-1614.

Broxson, C., Beckett, J. & Tornaletti, S. (2011). Transcription arrest by a G quadruplex forming-trinucleotide repeat sequence from the human c-myb gene. *Biochemistry 50*: 4162-4172.

Christudoss, P., Selvakumar, R., Fleming, J. J. & Gopalakrishnan, G. (2011) Zinc status of patients with benign prostatic hyperplasia and prostate carcinoma. *Indian J Urol 27*: 14-18.

Delaglio, F., Grzesiek, S., Vuister, G. W., Zhu, G., Pfeifer, J. & Bax, A. (1995). NMRPipe: a multidimensional spectral processing system based on UNIX pipes. *J Biomol NMR 6*: 277-293.

Elrod-Erickson, M., Rould, M. A., Nekludova, L. & Pabo, C. O. (1996). Zif268 protein-DNA complex refined at 1.6 A: a model system for understanding zinc finger-DNA interactions. *Structure 4*: 1171-1180.

Franzle, S. & Markert, B. (2003). Carcinogenesis and chemotherapy viewed from the perspective of stoichiometric network analysis (SNA): what can the biological system of the elements contribute to an understanding of tumour induction by elemental chemical noxae (e.g., Ni2+ , Cd2+) and to an understanding of chemotherapy? *ScientificWorldJournal 3*: 319-341.

Frisch, M. J. T., G. W.; Schlegel, H. B.; Scuseria, G. E.; Robb, M. A.; Cheeseman, J. R.; Montgomery, Jr., J. A.; Vreven, T.; Kudin, K. N.; Burant, J. C.; Millam, J. M.; Iyengar, S. S.; Tomasi, J.; Barone, V.; Mennucci, B.; Cossi, M.; Scalmani, G.; Rega, N.; Petersson, G. A.; Nakatsuji, H.; Hada, M.; Ehara, M.; Toyota, K.; Fukuda, R.; Hasegawa, J.; Ishida, M.; Nakajima, T.; Honda, Y.; Kitao, O.; Nakai, H.; Klene, M.; Li, X.; Knox, J. E.; Hratchian, H. P.; Cross, J. B.; Bakken, V.; Adamo, C.; Jaramillo, J.; Gomperts, R.; Stratmann, R. E.; Yazyev, O.; Austin, A. J.; Cammi, R.; Pomelli, C.; Ochterski, J. W.; Ayala, P. Y.; Morokuma, K.; Voth, G. A.; Salvador, P.; Dannenberg, J. J.; Zakrzewski, V. G.; Dapprich, S.; Daniels, A. D.; Strain, M. C.; Farkas, O.; Malick, D. K.; Rabuck, A. D.; Raghavachari, K.; Foresman, J. B.; Ortiz, J. V.; Cui, Q.; Baboul, A. G.; Clifford, S.; Cioslowski, J.; Stefanov, B. B.; Liu, G.; Liashenko, A.; Piskorz, P.; Komaromi, I.; Martin, R. L.; Fox, D. J.; Keith, T.; Al-Laham, M. A.; Peng, C. Y.; Nanayakkara, A.; Challacombe, M.; Gill, P. M. W.; Johnson, B.; Chen, W.; Wong, M. W.; Gonzalez, C.; and Pople, J. A.; (2004). Gaussian 03. Gaussian. Wallingford, CT, Gaussian. Inc. *Revision D.02*.

Gamsjaeger, R., Liew, C. K., Loughlin, F. E., Crossley, M. & Mackay, J. P. (2007). Sticky fingers: zinc-fingers as protein-recognition motifs. *Trends Biochem Sci 32*: 63-70.

Ghosh, S., Salsbury, F. R., Jr., Horita, D. A. & Gmeiner, W. H. (2011). Zn2+ selectively stabilizes FdU-substituted DNA through a unique major groove binding motif. *Nucleic Acids Res 39*: 4490-4498.

Gmeiner W.H., R. W. C., and Pommier Y. (2010). Genome-Wide mRNA and MicroRNA Profiling of the NCI 60 Cell-Line Screen and Comparison of FdUMP[10] with Fluorouracil, Floxuridine, and Topoisomerase1 Poisons. *Molecular Cancer Theraputics 9*: 3105 - 3114.

Gmeiner, W. H. (2005). Novel chemical strategies for thymidylate synthase inhibition. *Curr Med Chem 12*: 191-202.

Gmeiner, W. H., Salsbury, F., Jr., Olsen, C. M. & Marky, L. A. (2011). The stability of a model substrate for topoisomerase 1-mediated DNA religation depends on the presence of mismatched base pairs. *J Nucleic Acids*: 631372.

Hartwig, A. (2010). Mechanisms in cadmium-induced carcinogenicity: recent insights. *Biometals 23*: 951-960.

Kelleher, S. L., McCormick, N. H., Velasquez, V. & Lopez, V. (2011). Zinc in specialized secretory tissues: roles in the pancreas, prostate, and mammary gland. *Adv Nutr 2*: 101-111.

Lee, J. S., Latimer, L. J. & Reid, R. S. (1993). A cooperative conformational change in duplex DNA induced by Zn2+ and other divalent metal ions. *Biochem Cell Biol 71*: 162-168.

Lewis, E. A., Munde, M., Wang, S., Rettig, M., Le, V., Machha, V. & Wilson, W. D. (2011). Complexity in the binding of minor groove agents: netropsin has two thermodynamically different DNA binding modes at a single site. *Nucleic Acids Res 39*: 9649-9658.

Liao, Z. Y., Sordet, O., Zhang, H. L., Kohlhagen, G., Antony, S., Gmeiner, W. H. & Pommier, Y. (2005). A novel polypyrimidine antitumor agent FdUMP[10] induces thymineless death with topoisomerase I-DNA complexes. *Cancer Res 65*: 4844-4851.

Nelson, S. M., Ferguson, L. R. & Denny, W. A. (2007). Non-covalent ligand/DNA interactions: minor groove binding agents. *Mutat Res 623*: 24-40.

Pardee, T. S., Gomes, E., Jennings-Gee, J., Caudell, D. & Gmeiner, W. H. (2012). Unique dual targeting of thymidylate synthase and topoisomerase1 by FdUMP[10] results in high efficacy against AML and low toxicity. *Blood 119*: 3561-3570.

Sklenar, V., Piotto, M., Leppik, R. & Saudek, V. (1993). Gradient-Tailored Water Suppression for H-1-N-15 Hsqc Experiments Optimized to Retain Full Sensitivity. *Journal of Magnetic Resonance Series A 102*: 241-245.

Soderlind, K. J., Gorodetsky, B., Singh, A. K., Bachur, N. R., Miller, G. G. & Lown, J. W. (1999). Bis-benzimidazole anticancer agents: targeting human tumour helicases. *Anticancer Drug Des 14*: 19-36.

Spring, B. Q. & Clegg, R. M. (2007). Fluorescence measurements of duplex DNA oligomers under conditions conducive for forming M-DNA (a metal-DNA complex). *J Phys Chem B 111*: 10040-10052.

Uzzo, R. G., Leavis, P., Hatch, W., Gabai, V. L., Dulin, N., Zvartau, N. & Kolenko, V. M. (2002). Zinc inhibits nuclear factor-kappa B activation and sensitizes prostate cancer cells to cytotoxic agents. *Clin Cancer Res 8*: 3579-3583.

Van Hecke, K., Nam, P. C., Nguyen, M. T. & Van Meervelt, L. (2005). Netropsin interactions in the minor groove of d(GGCCAATTGG) studied by a combination of resolution enhancement and ab initio calculations. *Febs J 272*: 3531-3541.

Yang, Z. & Hayes, J. J. (2011). The divalent cations Ca2+ and Mg2+ play specific roles in stabilizing histone-DNA interactions within nucleosomes that are partially redundant with the core histone tail domains. *Biochemistry 50*: 9973-9981.

Zimmer, C., Marck, C., Schneider, C. & Guschlbauer, W. (1979). Influence of nucleotide sequence on dA.dT-specific binding of Netropsin to double stranded DNA. *Nucleic Acids Res 6*: 2831-2837.

Zimmer, C., Puschendorf, B., Grunicke, H., Chandra, P. & Venner, H. (1971). Influence of netropsin and distamycin A on the secondary structure and template activity of DNA. *Eur J Biochem 21*: 269-278.

Figures :

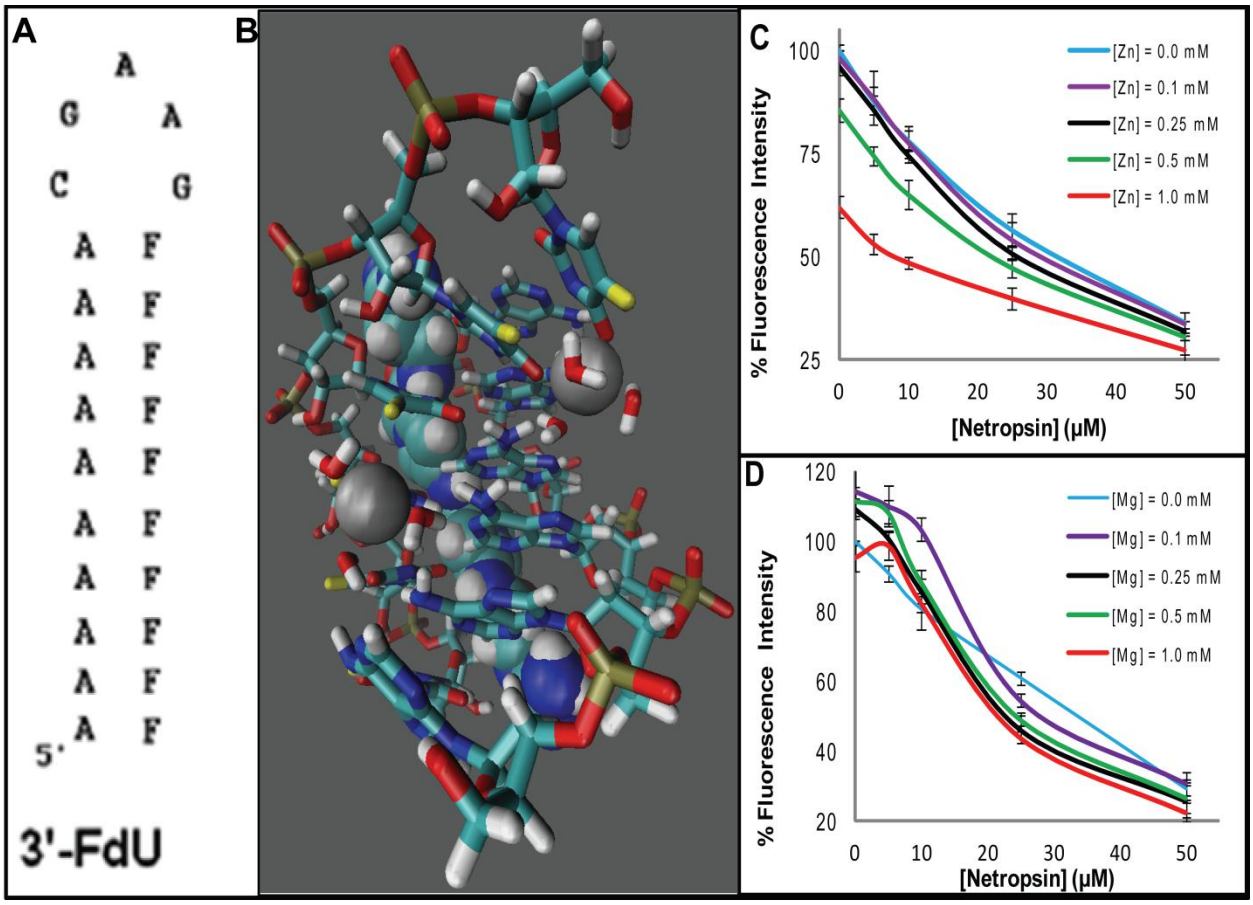

Figure 1 – (a) Structure of 3'FdU - the DNA hairpin investigated in the present studies. (b) Computationally-derived model of hemi-deprotonated 3'FdU hairpin complexed with netropsin in the minor groove and Zn^{2+} in the major groove. (c) Zn^{2+}, but not Mg^{2+}, enhances EtBr exclusion in combination with netropsin. EtBr exclusion data graphed as fluorescence intensity of EtBr bound to complex of 3'FdU to 0 – 1mM Zn^{2+} (or Mg^{2+}) and 0 – 50μm netropsin. The fluorescence intensity of the complex is normalized to fluorescence intensity for EtBr bound to 3'FdU only.

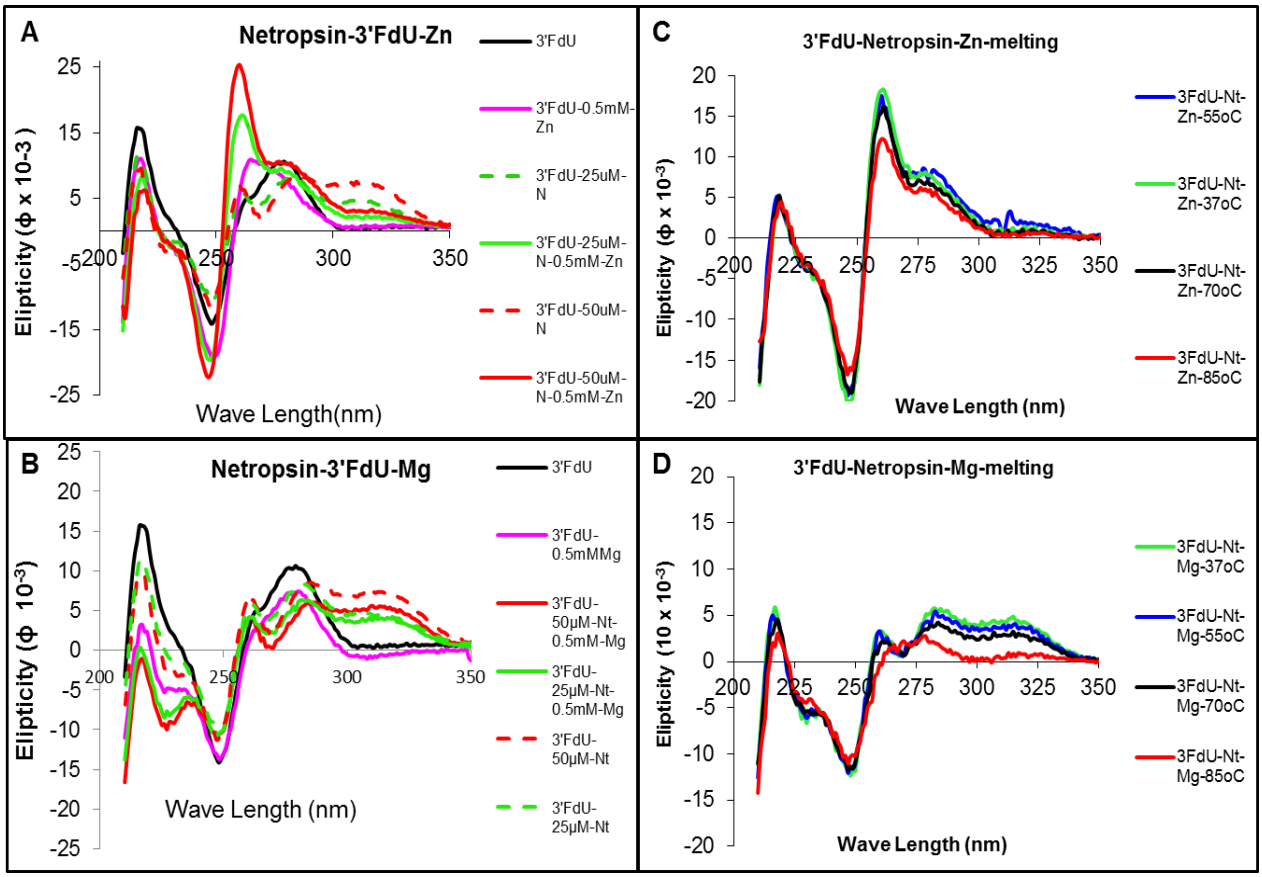

Figure 2 – CD spectra demonstrate Zn^{2+} selectively induces a blue-shift and intensity enhancement for the absorption maximum (280 -> 260 nm) in combination with netropsin upon binding to 3'FdU. Spectra were acquired in the presence or absence of Zn^{2+}/ Mg^{2+} and netropsin at the indicated concentrations. (a) CD spectra of 3'FdU and 0, 25, 50 μM Netropsin and 0, 0.5 mm Zn^{2+}. (b) CD spectra of 3'FdU and 0, 25, 50 μM Netropsin and 0, 0.5 mm Mg^{2+}. (c) CD spectra of Zn^{2+}/netropsin:3'FdU at indicated temperatures. (d) CD spectra of Mg^{2+}/netropsin:3'FdU at indicated temperatures.

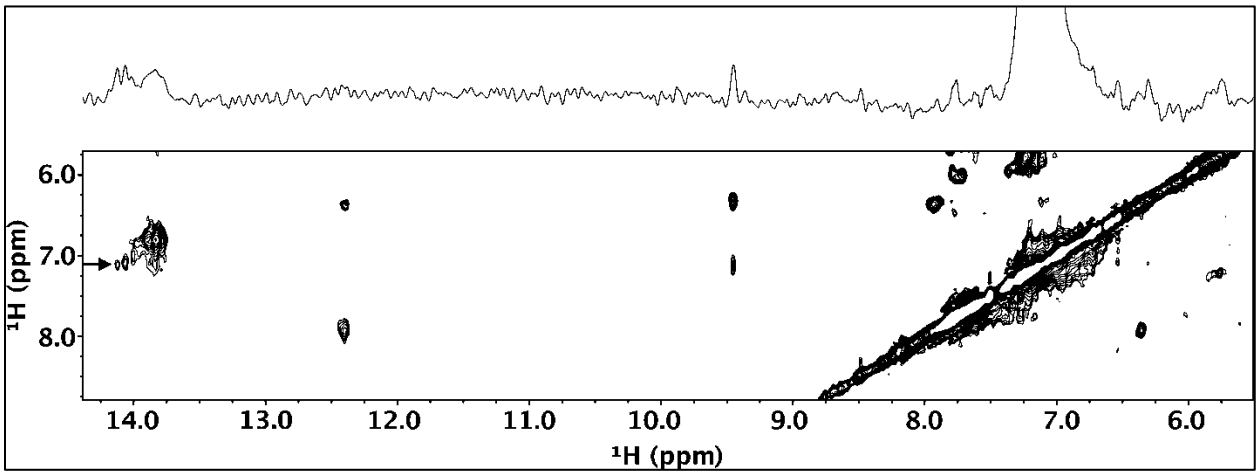

Figure 3 – Overlay of 2D NOESY NMR spectrum for 3'FdU (grey) and Zn^{2+}/netropsin:3'FdU (red). The region shown includes the aromatic 1H resonances of adenine. Arrows denote the location of AH2 resonances that give NOEs both to other AH2 resonances and to netropsin 1H resonances for Zn^{2+}/netropsin:3'FdU (red) but not for 3'FdU (grey). The results are consistent with netropsin binding 3'FdU in the minor groove and enhancing base stacking among adjacent adenines.

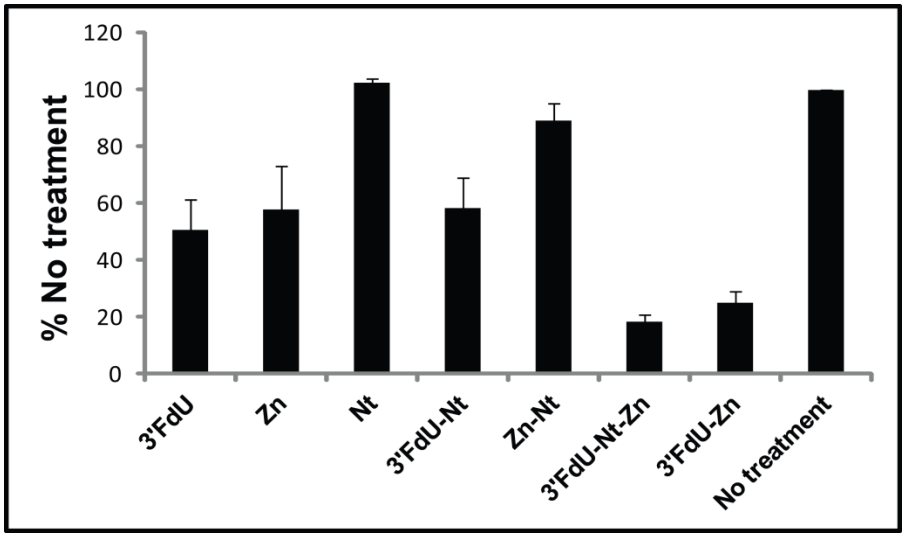

Figure 4 – MTS assay readout of a modified clonogenic assay demonstrating enhanced cytotoxicity for Zn^{2+}/netropsin:3'FdU relative to the constituent components towards PC3 prostate cancer cells. Netropsin is slightly growth stimulatory towards PC3 cells while Zn^{2+} enhances the cytotoxicity of 3'FdU towards these cells.

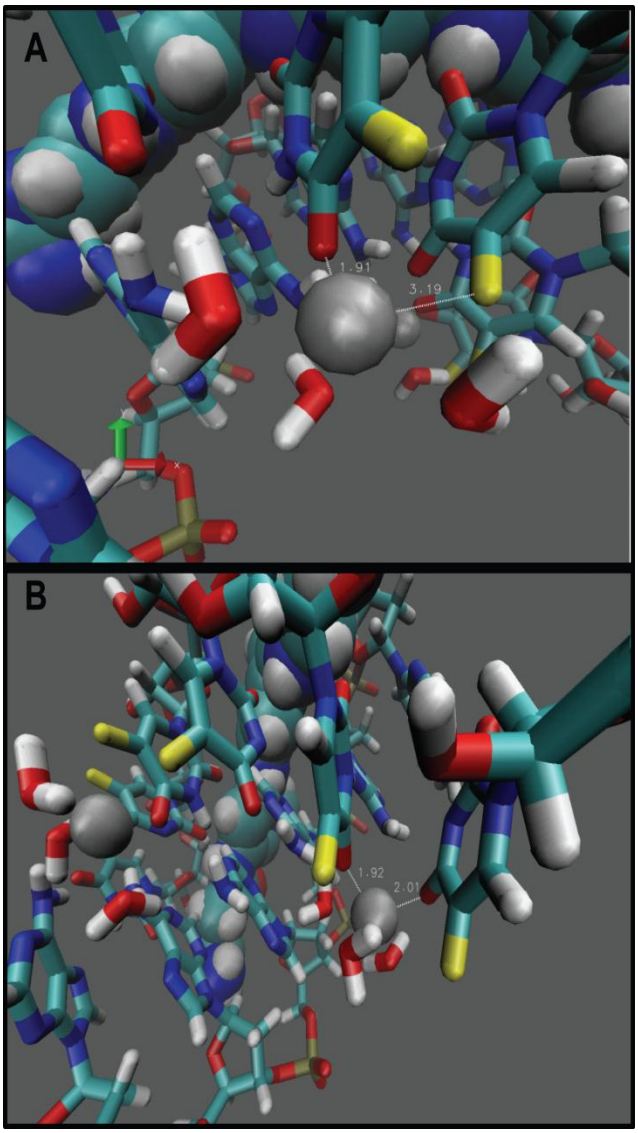

Figure 5 – (a) Computationally-derived model for site 1 Zn^{2+} complexation to the hemi-deprotonated 3'FdU hairpin in combination with netropsin. Zn^{2+} is located in the major groove with a distorted trigonal bipyramidal geometry in which the fluorine from the deprotonated FdU is one axial ligand and O4 from the second FdU is the second axial ligand. Water molecules are the equatorial ligands. White dashed lines are used to illustrate the coordinating atoms. (b) Model for site 2 Zn^{2+} complexation depicting partial covalent interactions from O4 from consecutive FdU nucleotides with Zn^{2+}.

Appendix #2 – manuscript in preparation

Selective Delivery of Doxorubicin to PSMA+ Prostate Cancer Cells Using a Novel Dimeric DNA Aptamer Construct

Authors (alphabetical): Olcay Boyacioglu, Christopher Stuart (others?)

Corresponding Author: William H. Gmeiner

Department of Cancer Biology and Program in Molecular Medicine, Wake Forest School of Medicine, Winston-Salem, NC 27157

(336)716-6216; bgmeiner@wakehealth.edu

Running Title: Dimeric Aptamer Complex for Selective Doxorubicin Delivery.

Key Words: PSMA, Aptamer, Chemotherapy, Prostate Cancer

Abstract: Treatment with Doxorubicin (Dox) results in serious systemic toxicities that limit effectiveness for cancer treatment and cause long-term health issues for cancer patients treated with this widely used anti-cancer drug. We have identified a new DNA aptamer to prostate specific membrane antigen (PSMA) and have developed dimeric aptamer complexes for specific delivery of Dox to PSMA+ cancer cells. The dimeric aptamer complexes are stable under physiological conditions and internalized specifically into $PSMA^+$ C4-2 cells with minimal uptake into PSMA-null PC3 cells. Cellular internalization of the dimeric complex was demonstrated by confocal microscopy and flow cytometry. Dox was covalently bound to the dimer complex with stoichiometry 4:1 using a reversible linker that promotes covalent attachment of Dox to genomic DNA following cell internalization. Dox was released from the complex under physiological conditions with a half-life of 8 h, sufficient for *in vivo* targeting. The dimeric aptamer complex was used to selectively deliver Dox to C4-2 cells with endosomal release and nuclear localization of Dox. The covalent Dox:aptamer complex was selectively cytotoxic to C4-2 cells with similar cytotoxicity as the molar equivalent of free Dox. In contrast the Dox:aptamer complex displayed minimal cytotoxicity to PC3 cells demonstrating the dimeric aptamer complex displays a high-degree of selectivity for $PSMA^+$ cells. The dimeric aptamer complex displays specificity and stability features that may be useful for improved delivery of Dox selectively to malignant tissue *in vivo*.

Introduction

Prostate specific membrane antigen (PSMA) is of interest for selective delivery of therapeutics for cancer treatment as a consequence of its elevated expression on the apical plasma membrane[1] of prostate cancer cells and in endothelial cells of vasculature from diverse malignancies. PSMA is an exopeptidase[2] with folate hydrolase and NAALDase activities. PSMA also associates with anaphase promoting complex and its expression may promote aneuploidy.[3] PSMA is expressed by prostate epithelial cells,[4] however elevated PSMA expression occurs in advanced PCa including bone metastases.[5] PSMA expression levels are an independent predictor of PCa recurrence.[6] PSMA is also expressed in vasculature[7] from many different cancers including a high percentage of bladder[8], gastric and colorectal[9], as well as hepatocellular, renal, breast and ovarian cancer.[2] PSMA is expressed as a dimer[10], and dimerized ligands targeting the PSMA-dimer display improved activity relative to monovalent ligands.[11]

The restricted expression of PSMA has resulted in numerous attempts to both image and treat cancer with PSMA-targeted diagnostic and therapeutic modalities. Three classes of molecules have been most frequently employed in these targeted applications: mAbs such as J591, RNA aptamers such as A10-3, and small molecule inhibitors of PSMA enzymatic activity. Radiolabeled conjugates of J591 are being investigated for treatment of advanced PCa[12] and have been utilized for cancer imaging. PSMA inhibitors have been used to deliver theranostic NPs to cancer cells.[13] The A10-3 RNA aptamer to PSMA has been used to deliver diverse therapeutic modalities selectively to cancer cells including cisplatin,[14, 15] functionalized nanoparticles,[16] a micelle encapsulated PI3K-inhibitor,[17] as well as toxins[18] and siRNA[19],[20]. Aptamer-targeting of PSMA may be particularly beneficial for delivery of

anti-cancer drugs that have serious systemic toxicities, such as doxorubicin (Dox), and several reports have demonstrated cancer cell specific delivery of Dox using RNA aptamers. Dox was non-covalently bound to a dual-aptamer complex that included A10-3 and targeted to PCa cells.[21] Dox also was non-covalently bound to A10-3 and conjugated to super paramagnetic iron oxide nanoparticles (NPs) and to gold NPs.[22]

The current approaches to Dox delivery using RNA aptamers have several limitations that may be overcome to improve treatment outcomes. Current RNA aptamers are costly to produce and require use of modified nucleotides for nuclease stability. Two groups recently described modifications to the A10-3 RNA aptamer to create truncated versions that target PSMA efficiently but that are less costly to produce.[23],[24]. In contrast to these approaches, we describe herein the identification of a new DNA aptamer to PSMA that is efficiently synthesized in a cost-effective manner and that can be rendered nuclease-resistant by introduction of a single non-standard (3'-3') linkage. Another limitation of the current approaches for aptamer-mediated Dox delivery is the manner in which Dox is associated with the aptamer complex. Most recently described approaches have utilized Dox non-covalently associated with an RNA aptamer. Non-covalent complexes of Dox with duplex DNA have limited stability with half-lives of only a few minutes or less and it is unlikely that non-covalent complexes of Dox with aptamers would be sufficiently stable for optimal *in vivo* activity. We describe herein covalent complexes of Dox with a novel dimeric construct of our DNA aptamer that includes two CpG sequences that both improve thermal stability and reduce nuclease sensitivity. CpG is the preferred sequence for Dox binding and we demonstrate covalent attachment of Dox via a formaldehyde linkage which results in stable complexes with half-lives of several hours suitable for *in vivo* application and that promotes binding to genomic DNA following cellular internalization of the dimeric aptamer complex.

Material and Methods

DNA SELEX. Recombinant human PSMA extracellular domain (720 amino acids; x-y) was expressed from baculovirus (Kinakeet Biotechnology; Richmond, VA). The recombinant protein was used to form an affinity matrix using Talon beads which was then used in a DNA SELEX procedure to identify DNA aptamers to PSMA. DNA aptamers were selected from a library including a 47 nucleotide random sequence flanked by priming sequences of 21 nucleotides each:

dGCGAAAACGCAAAAGCGAAAA(N47)ACAGCAATCGTATGCTTAGCA

Initially 8 ug ssDNA from the random library (307 picomoles of DNA; 186 trillion sequences) was converted to dsDNA using a T7 fill-in reaction and amplified by PCR using a 5'-primer that included a 5'-phosphate. The resulting dsDNA was converted to ssDNA using λ-exonuclease selectively cleaving the strand amplified with the phosphorylated primer. SELEX forward rounds were performed by adding 1 mg of PSMA-bound to Dynabeads Talon to 700 μL of binding buffer (100 mM NaCl, 20 mM Tris, 2 mM MgCl2, 5 mM KCl, 1 mM CaCl2, 0.2% Tween-20, pH 8). The beads were removed using a xx magnet and washed four times with binding buffer. At least 10 μg of ssDNA was annealed by heating to 95 °C followed by cooling and refrigeration was added to the PSMA-matrix followed by gentle vortexing and incubation for 1 h at 37 °C with gentle shaking. The supernatant was removed and 20 μL of 5 uM 5'-phosphorylated primer was added to the beads and the mixture was heated to 95 °C for 5 min following which the beads were sequestered and the supernatant transferred to a clean microfuge tube and DNA converted to dsDNA using a primer-extension reaction using T7 polymerase. DNA was collected by ethanol precipitation and then amplified by 10 cycles of PCR using a phosphorylated 3'-primer. The dsDNA was

purified by gel electrophoresis followed by ethanol precipitation and then converted to ssDNA by treating 32-40 μg of dsDNA with λ-exonuclease in λ-buffer () for 30 min at 37 °C followed by ethanol precipitation. The resulting ssDNA was analyzed by gel electrophoresis and quantified by UV absorbance and used in a subsequent SELEX forward or counter round. Counter rounds differed from forward rounds by incubation with a magnetic bead matrix that did not contain PSMA and using the DNA that did not bind to the matrix for subsequent PCR amplification. A total of 10 forward and two counter rounds were performed. After the final SELEX round, ssDNA was converted to dsDNA using a T7 fill-in procedure and was cloned into a pGEM vector (Promega) for sequencing. A single, 48 nucleotide sequence (SZTI01) was identified and used in subsequent studies.

SZTI01: dGCGTTTTCGCTTTTGCGTTTTGGGTCATCTGCTTACGATAGCAATGCT

Dimeric Aptamer Complexes:

Results

Thermal Stability of Dimeric Aptamer Complexes. A key design feature for our strategy for covalent delivery of Dox to PCa cells was the formation of a duplex DNA "bridge" linking the two DNA aptamers (**Figure**). The bridging DNA duplex should be sufficiently stable thermally such that the dimeric aptamer complex remains intact under physiological conditions for times sufficient for aptamers to localize specifically to targets *in vivo*. Thermal melting profiles were obtained for dimeric aptamer complexes composed of two DNA aptamers each of which included a ssDNA sequence, either dA_{16} or T_{16}, appended to the 3'-terminus (**Figure**). The temperature-dependent UV melting profile for the dimeric complex indicated initial dissociation occurred at 41 °C with a melting temperature of 47 °C. While melting for this complex occurred above physiological temperature, somewhat increased stability for the dimeric aptamer complex would be preferred to promote long-term stability under physiological conditions. Further, the A-T duplex used to form this dimeric complex did not include a preferred Dox-binding sequence motif. We prepared an alternative dimeric aptamer complex by appending GCCG and CGGC sequences to the 5'- and 3'-ends of the DNA duplex forming sequences dA_{16} and T_{16}. The resulting duplexes displayed initial dissociation at 54 °C with a melting temperature of 58 °C, thus displaying stability suitable for further development. C3 – include?

Dox vs 670 dot plot (4:1 ratio? How uniform?))

Formation and Dissociation of Covalent Dox-Conjugates. The duplex DNA binding motif introduced into the dimeric aptamer complex has the potential for binding two equivalents of Dox per complex. In addition, the DNA aptamers comprising the complex contain other

potential sites of Dox binding. We reacted the dimeric complex with a four-fold excess of Dox in the presence of formaldehyde and evaluated the amount of Dox bound in the complex by dissociation at acidic pH upon heating. The ratio of Dox to dimeric complex was 4:1 (**Figure**). To assess to what extent formation of the covalent linkage via formaldehyde resulted in enhanced stability for the covalent complex relative to non-covalent binding, the half-life for the complex was evaluated using a fluorescence transfer assay. These studies revealed the half-life for Dox covalently bound via formaldehyde was > 8 h while the half-life for the non-covalent complex was < 30 min (**Figure**). These studies indicated that covalent attachment of Dox results in formation of a complex with increased retention of Dox that is well-suited for drug-delivery applications *in vivo*.

PSMA-Specific Uptake of Dimeric Complexes. The selective delivery of Dox to $PSMA^+$ cells requires binding and ideally internalization of the complex. To evaluate to what extent the dimeric aptamer complex was specific for binding and internalization into $PSMA^+$ cells, we compared internalization of the complex in $PSMA^+$ C4-2 cells and PSMA-null PC3 cells using confocal microscopy and flow cytometry. The component of the dimeric complex containing dA_{16} ssDNA was labeled with Quasar570 while the component with T_{16} ssDNA was labeled with Quasar 670 permitting simultaneous detection and visualization of each aptamer component. Confocal microscopy revealed minimal uptake of either fluorescently-labeled aptamer into PC3 cells however strong signal was observed for each fluorescent aptamer signal in $PSMA^+$ C4-2 cells (**Figure**). Further, fluorescence emitted from each of the two aptamers was completely co-localized consistent with uptake and retention of the dimeric complex in dimeric form. Fluorescence emitted from the aptamer complexes appeared punctate, consistent with endosomal localization of the dimeric complex. There was no evidence for nuclear localization of the aptamer complex. To confirm fluorescence

resulted from dimeric complex that had been internalized into C4-2 cells, *z*-stack images were obtained and confirmed the complex was internalized and not surface-bound.

The internalization of dimeric aptamer complex into PC3 and C4-2 cells was further investigated using flow cytometry. In these studies, we also compared to what extent inclusion of a flexible linker might enhance cell uptake. The results are shown in **Figure**. Significant internalization of fluorescence was observed for both of the dimeric aptamer complexes in C4-2 cells while PC3 cells displayed (significantly) reduced signal). Similar fold-levels of fluorescence uptake selectivity were detected for both 570 and 670 nm detection although absolute signal levels were higher for 670 nm fluorescence due to the fluorescence detection configuration of the flow cytometer. Inclusion of the flexible linker did not significantly impact cellular uptake in these studies.

PSMA-Specific Delivery of Dox. The specific delivery of Dox to $PSMA^+$ cells via the dimeric aptamer complex was evaluated using confocal microscopy. While non-complexed Dox readily accumulates in the nuclei of both PC3 and C4-2 cells, Dox associated with the dimeric aptamer complex is nearly exclusively internalized into C4-2 cells with minimal accumulation in PC3 cells. Dox signal was exclusively nuclear while signal from the aptamer displayed nuclear exclusion consistent with Dox becoming dissociated from the dimeric aptamer complex following cellular internalization. The results are consistent with Dox becoming dissociated in the acidic environment of the endosome following cell-uptake of the dimeric aptamer complex followed by nuclear localization free Dox. The results demonstrate that the dimeric aptamer complex promotes PSMA-specific uptake with nuclear delivery of Dox.

PSMA-Dependent Selective Cytotoxicity. The utility of the dimeric aptamer complexes for PSMA-specific cytotoxicity was evaluated using cell-viability assays with PC3 and C4-2 cells following treatment with the dimeric aptamer complex. The results are shown in **Figure**. Dox-alone was highly cytotoxic to both PC3 and C4-2 cells consistent with the wide-spectrum activity previously reported for Dox. In contrast, Dox complexed with the dimeric aptamer was only highly cytotoxic towards C4-2 cells but displayed greatly reduced cytotoxicity to PC3 cells. The results indicate that in the context of the dimeric aptamer complex, Dox displays similar cytotoxicity as the molar equivalent of free-Dox towards C4-2 cells indicating that the potency of Dox is preserved in the context of the dimeric aptamer complex. In contrast, the dimeric aptamer complex is highly protective of PC3 cells with Dox displaying minimal cytotoxicity.

Discussion

Aptamer-mediated delivery is a promising strategy for improving the therapeutic index of cytotoxic drugs that cause serious systemic toxicities, such as Dox. Aptamers may be prepared more cost-effectively relative to mAbs and are more amenable to chemical dervatization for drug-delivery applications. PSMA has emerged as a favored target for aptamer-mediated delivery of cytotoxic drugs and NPs because of its elevated expression in advanced prostate cancer and in the vasculature of diverse malignancies. The majority of studies described for PSMA-targeting with aptamers have used variants of the A10 RNA aptamer. While these studies have been successful, the utility of these aptamers may be limited by cost and nuclease sensitivity. We describe a new dimeric DNA aptamer.
The studies described to date have

References

Appendix #3 – Manuscript in Preparation

Synthesis of Doxorubicin:DNA Hairpin Conjugates With Therapeutic Potential as Controlled-Release Multi-modality Drug Delivery Systems

Christopher H. Stuart[1,2], David A. Horita[3], Michael J. Thomas[3], Freddie R. Salsbury Jr [4], Mark O. Lively[3], William H. Gmeiner[1,2]*

[1]Department of Cancer Biology, [2]Department of Molecular Medicine and Translation Science, Wake Forest School of Medicine, [3]Department of Biochemistry, Wake Forest School of Medicine, Winston-Salem, NC 27157, and [4]Department of Physics, Wake Forest University, Winston-Salem, NC 27109

Abstract: Doxorubicin (Dox) is a commonly used chemotherapeutic with dose-limiting cardiotoxicity. Herein we describe the selective chemical reactivity for a single guanine in the context of a 25mer DNA hairpin to form a covalent complex with Dox. 2D ^{1}H-^{15}N NMR and mass spectrometry were used to verify the selective chemical reactivity. The resulting DNA:Dox hairpin (DDH) displays markedly enhanced stability relative to alternative complexes and thus may be useful for drug delivery applications. DDH may be also used to incorporate additional cytoxic elements, such as fluorinated bases and may also be targeted to malignant cells to reduce the side-effects associated with Dox treatment.

Doxorubicin (Dox) is widely-used as a chemotherapeutic for the treatment of diverse malignancies, including breast and prostate cancer. Serious toxicities, including an occasionally lethal cardiotoxicity, restrict the therapeutic utility of Dox, and have resulted in a search for chemical modifications that attenuate systemic toxicities while maintaining strong anti-tumor activity. We describe a new approach that takes advantage of the selective chemical reactivity of a single-site in a DNA hairpin to create novel Dox:DNA hairpin:drug conjugates (DDH). These DDH may also be used as a scaffold for delivering cytotoxic nucleotides, such as 5-fluoro-2'-deoxyuridine (FdU) and may be targeted to malignant cells through chemical conjugation with folate, biotin, or other moieties.

Dox can form both non-covalent and covalent complexes with duplex DNA with the covalent complexes being more stable and requiring an aldehyde precursor to link the daunosamine sugar of Dox to the exocyclic amine of guanine with the reaction proceeding via a Schiff base intermediate.[1,2] General features for both the non-covalent and covalent complexes of Dox with DNA include intercalation of the tetracene ring system and occupation of the minor groove by the daunosamine sugar moiety[3]. Dox bound to genomic DNA acts as a Topoisomerase II (TopII) poison[4,5] and this is primarily responsible for the anti-tumor activity of Dox. Dox covalent binding to DNA occurs with sequence specificity for 5'-dGpC sites, suggesting a 3D conformation that facilitates the covalent attachment at these sites[6].

Dox:DNA covalent adducts have been synthesized and used as end-points in studies of anthracycline cytotoxicity[7], however there is no reason in principle why DNA cannot be used as a delivery vehicle for Dox. As far as we are aware, no previous studies have explored the

formation of Dox:DNA conjugates in non-conventional DNA structures or have assessed the potential of these conjugates to deliver Dox to malignant cells. Herein, we describe the synthesis of two DDH's where the amine of the duanosamine sugar of Dox is covalently bound to the N2-amino of dG in a hairpin loop through a single CH_2 linker derived from formaldehyde. Our studies utilized a 25mer oligodeoxynucleotide hairpin consisting of a GAA intramolecular hairpin-promoting sequence motif closed by a CG base pair with a stem consisting of either 10 dA-dT (TDDH) or dA-FdU (FDDH) base pairs. Intramolecular hairpin formation was favored over dimerization by heating and flash-cooling of the DNA. The DNA hairpin readily reacts with Dox in aqueous solution in the presence of formaldehyde. The resulting covalent adduct is isolated from excess Dox and formaldehyde by chloroform extractions and ethanol precipitation. Yields are typically 70-80% for the conjugate as measured by UV absorbance at 260nm for both the FDDH and TDDH. No further effort was made to isolate unreacted DNA as spectroscopic analysis suggested the reaction went to completion (see Supporting Information). These spectroscopic analyses showed a 1:1 molar ratio of Dox:DNA. ESI-QTOF mass spectroscopy of FDDH confirmed the reaction of Dox to DNA with the addition of a single CH_2 linker derived from the formaldehyde in 1:1 stoichiometry (Fig 1A).

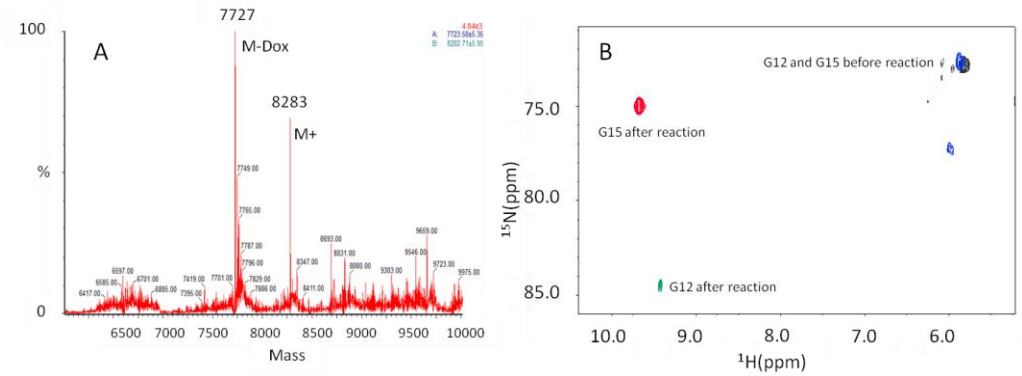

Figure 1. A) M-Dox peak of MW 7723 corresponds to the un-reacted parent DNA, while M+ peak of MW 8283 is obtained by the addition of Dox (MW 543) and CH_2 (MW 14). B) Overlay of ^{1}H-^{15}N HSQC displaying the N2 of G12 and G15 from two independent singly-labeled samples. Blue and green peaks represent the G12 amino before and after reaction with Dox, respectively. Black and red peaks represent the G15 amino before and after reaction respectively.

Guanines have been shown previously to be the preferred site for covalent adduct formation of DNA with Dox. To determine to what extent the two non-equivalent guanines (G12 or G15 – Figure 2) in our DNA hairpins displayed differential reactivity towards Dox the non-fluorinated DNA hairpin TDDH was site-specifically labeled with ^{15}N at G12 and G15 through two independent syntheses. Specific-labeling was achieved by synthesizing the oligomers with 1:4 ratio of the ^{15}N labeled guanine to unlabeled guanine resulting in two hairpins, each singly-labeled at either G12 or G15. These ^{15}N-labeled DNA hairpins were each separately reacted and the covalent complexes were studied with ^{15}N-edited 2D NMR to determine the site of reactivity (^{1}H NMR available in Supporting Information). ^{15}N-labeling both simplified the spectral assignments and also provided additional chemical information about the reactive site (Fig 1B).

The N2 aminos for G12 and G15 in the unreacted hairpin each displayed nitrogen shifts at 72.64 and 72.81ppm respectively and hydrogen shifts at 5.89 and 5.83ppm, consistent with previous reports[8]. A second peak with a nitrogen shift of 77.20 and a hydrogen shift of 5.98ppm likely resulted from a small amount of contaminating DNA dimers that formed at the high concentrations of DNA needed for NMR spectroscopy. Upon reaction with Dox/formaldehyde the G12 and G15 aminos displayed considerably different chemical shifts. The G15 amino in the covalent complex is shifted slightly to 74.98ppm with the corresponding ^{1}H shifted to 9.67ppm. In contrast, the G12 amino undergoes a substantial nitrogen shift to 84.48ppm with ^{1}H resonances at 9.67ppm. The nitrogen shifts are consistent with a covalent modification at the amino of G12, and not G15.

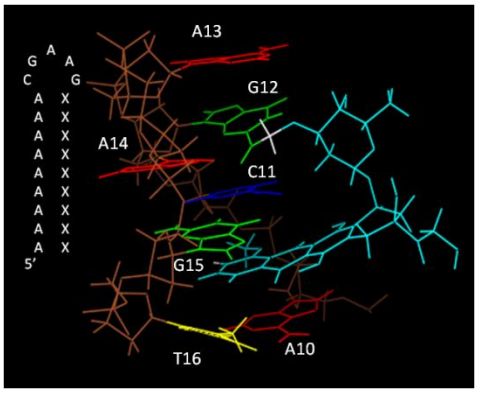

Figure 2. Secondary structure and working model of the DDH molecular structure, (X= FdU or dT). Dox is bound to N2 of G12 and intercalated between the G15:C11 and A10:T16 base pairs. The lower 9 AT base pairs of the stem have been truncated for simplicity. Structures are colored as follows; guanine:green, adenine:red, thymine:yellow, cytosine:blue, Dox:light blue, methylene linker:white, DNA backbone:brown

We then sought to create a working model for the structure of the DDH molecule using the data collected from the ^{15}N-edited 2D NMR using a structure of the hairpin loop characterized by Ulyanov et al[9] as the basis of our model. The hydrogen shifts of G15 could be caused by intercalation of Dox in the covalent complex, as shifts of amino protons to ≈10ppm have been attributed to increased hydrogen bonding in quadruplex DNA[10]. Preliminary data also showed the amino of G15 displayed several NOEs consistent with Dox localizing in the stem region of the hairpin. Pymol was used to edit the DNA from the previous NMR structure[9] to contain only the loop region and the first AT base pair. We then manipulated a model of Dox into a position that brought the aminos of G12 and Dox into close proximity, allowing for the formation of a methylene bridge between the aminos. This placement also allowed Dox to intercalate between the C11-G15 base pair and the first AT base pair in the stem of the DNA (Fig 2). This represents the first time that we are aware of that Dox covalent bonding has been observed in a hairpin loop region of DNA.

We hypothesized that covalent Dox attachment would allow for the DDH to serve as a Dox delivery molecule that may result in improved pharmacological properties and reduced systemic toxicities relative to conventional Dox. In order for the DDH to act as efficient delivery vehicles

they must be stable under physiological conditions, but also allow for Dox release and transfer to genomic DNA. We developed an assay that would quantify the transfer of Dox from the DDH to genomic DNA under physiologic conditions. This assay is based on the difference in fluorescence quenching for Dox in the context of the DDH relative to genomic DNA allowing us to quantify the ability of the DDH molecules to transfer Dox to genomic DNA. DDH, Dox, or the non-covalent hairpin+Dox were mixed with 100-fold excess of salmon sperm DNA (spDNA; w/w) to simulate genomic DNA. Reactions were allowed to incubate at 37°C with fluorescence quenching measured over a period of 48h. No fluorescence loss was observed in samples that lacked spDNA, while fluorescence was fully quenched within one hour of addition of spDNA for both free Dox and the non-covalent samples. Fluorescence quenching was significantly slowed for the DDH samples, with 50% quenching occurring around 30h for both TDDH and FDDH (see Supporting Information). Given that the non-covalent hairpin+Dox complex results in rapid quenching, intercalation into the hairpin is not solely responsible for the stability of the complex. However, covalent Dox dimers formed using formaldehyde have been shown to be readily hydrolysable under physiological conditions, resulting in complete disassociation of Dox and formaldehyde within ≈15min[11]. It is likely that a combination of intercalation and covalent bonding is responsible for the substantially lengthened time for Dox transfer from the DDH. We hypothesize that the covalent linkage acts as a tether between the Dox and DNA, and that when the bond is hydrolyzed intercalation holds the resulting amine and Schiff-base in close proximity allowing for them to reform the covalent linkage.

To our knowledge this is the first report of the use of a Dox-DNA covalent conjugate to transfer Dox to DNA for potential therapeutic applications, as well as the first combination of TopI and TopII poisons into a single molecule. This approach provides a means for delivering two synergistic therapeutics, Dox and the cytotoxic nucleotide 5-fluoro-2'-deoxyuridine-5'-O-monophosphate (FdUMP), through a single molecule, and at the same time potentially reducing the systemic toxicities of Dox as has been previously reported with lipid encapsulation[12]. Our laboratory has recently shown that Dox and the linear polymer FdUMP[10][13] are synergistic for treatment of acute myeloid leukemia (AML)[14] and the FDDH hairpin described herein provides an innovative system for co-delivering these two cytotoxic agents that comprehensively target topoisomerase 1 and 2, selectively to malignant cells. The DNA component of the DDH covalent complex could also be used as a scaffold for further conjugation with folate, biotin, or other moiteies to improve cell-specific uptake. Aptamers are currently being explored as a method for targeted Dox delivery[15,16], however, the current methods utilize only non-covalent complexes while our studies demonstrate the advantages of covalent conjugation to improve complex stability which may be particularly important for *in vivo* applications. Future studies will focus on demonstrating these advantages in cellular and animal models of cancer.

Experimental Section:

Synthesis of DDH: A 0.37% (by weight) solution of formaldehyde was prepared by dissolving an appropriate amount of paraformaldehyde in Dulbecco's Phosphate Buffered Saline without Calcium or Magnesium (DPBS) pH 7.4. Doxorubicin was added to either 4°C formaldehyde-PBS or PBS-alone to obtain a final Doxorubicin concentration of 250µM. DNA hairpin loops were prepared as previously reported[17] and added to the formaldehyde solution. Reactions were allowed to proceed at 10°C in the dark for 48 hours. DDH's were purified by extracting twice with phenol:chloroform and twice with chloroform. After extraction, DDH's were ethanol-precipitated and recovered by centrifugation. Pellets were rinsed twice with 100% ethanol and twice with 70% ethanol. Pellets were then evaporated to dryness. The red-pink pellets were then re-suspended in dH_2O. A Beckman Coulter DU 800 was used to measure absorption at 260nm. All products were stored at -20°C.

Doxorubicin:DNA conjugate ratio measurements: DNA samples were prepared to 10µM in dH_2O and absorbencies were measured from 200-800nm using a Beckman Coulter DU800 spectrophotometer. A standard curve of Dox was established between 1µM and 10µM by using absorbencies at 494nm. To assess the amount of Dox covalently bound to DNA the samples were heated to 85°C before measuring the absorbance at 494nm. The 260nm wavelength was used to determine the DNA content in the sample and to determine the Dox:DNA ratio.

Mass Spectrometry: Negative ion mass spectra were acquired using a Waters Q-TOF API-US mass spectrometer equipped with an Advion Nanomate source. Samples were diluted to about 5 µM with methanol: water: 2-propanol (49:49:2, v:v:v). Backing pressure and sprayer voltage were optimized for each analysis, but were usually about 0.8 psi and 1.2 kV, respectively. The cone voltage was 35V. The scan range from 525 *m/z* to 1600 *m/z* with an acquisition time of 1.2 s. Spectra were summed for 0.5 min for MaxEnt transform. The nucleotide GCATCCTGGAAAGCTACCTT, M^- = 6366.1, at 0.6 µM was used to monitor instrument performance. Spectra were analyzed using MassLynx 4.0.

NMR Spectroscopy: NMR samples were prepared in 50 mM sodium phosphate buffer, pH 7.0, with 10 % D_2O and a final volume of 250 µL All NMR spectra were acquired on a Bruker Avance 600 MHz spectrometer at 10 °C using a TXI Cryoprobe. NOESY spectra were acquired with a 100 µs mixing time and 3-9-19 Watergate[18] water suppression with a 220 ms interpulse delay. HSQC spectra were acquired using a 110 µs 3-9-19 interpulse delay and the ^{15}N transmitter set to 150 PPM for imino groups and to 75 PPM for amino groups (indirectly referenced to water at 4.7 PPM). Data were processed using NMRPipe[19] and analyzed using NMRView[20].

3D modeling of DDH: A PDB file of the hairpin molecule was obtained from the Protein Data Base under entry 1JVE[9]. A PDB file of Dox was obtained from the Protein Data Base under entry DM2. Files were loaded into Pymol, and the hairpin was modified to contain only 5'-ACGAAGT-3'. The models were then manipulated spatially to allow for a covalent bond to form between the N2 amino of G12 and the duanosamine of Dox. Hydrogens were added to the entire model using the molefacture plug in vmd[21]. The doxorubicin was then geometry optimized in the presence of the DNA using PM6[22] as implemented in Gaussian 09[23].

Dox transfer rate of DDH: Samples of 2.5µM DDH, Doxorubicin, or hairpin+Doxorubicin were prepared in DPBS with or without a 100-fold (by weight) excess of Salmon Sperm DNA and

incubated at 37°C. Fluorescence intensity was determined by Typhoon-9210 variable mode imager with excitation set to 532nm and the emission filter at 610nm.

Acknowledgements

The authors would like to thank the Michael Samuel from the Wake Forest University Mass Spectrometry Core Lab for his help in obtaining all of the mass spectrometry data used in this research. Oligonucleotide syntheses were performed in the DNA Synthesis Core Laboratory at Wake Forest University School of Medicine. The DNA Synthesis and the Mass Spectrometry Cores are part of the Bioanalytical Core Laboratory supported in part by the Comprehensive Cancer Center of Wake Forest University

Funding:

Department of Defense Prostate Cancer Research Program (093606 to W.H.G.) and the Comprehensive Cancer Center of Wake Forest University Cancer Center Support Grant P30 CA012197 supporting the Bioanalytical Core Laboratory. The Waters Q-TOF mass spectrometer was purchased with funds from NIH Shared Instrumentation Grant 1S10RR17846. MS analyses were performed in the Mass Spectrometer Facility of the Comprehensive Cancer Center of Wake Forest University School of Medicine supported in part by NCI center grant 5P30CA12197.

Supporting Information:UV-Vis spectra and Dox transfer rate graphs for both TDDH and FDDH and ^{1}H NMR for FDDH are available in the supporting information.

References:

1. Zeman, S. M.; Phillips, D. R.; Crothers, D. M. Characterization of covalent Adriamycin-DNA adducts. *Proc Natl Acad Sci U S A* **1998**, *95*, 11561–11565.
2. Cutts, S. M.; Parker, B. S.; Swift, L. P.; Kimura, K. I.; Phillips, D. R. Structural requirements for the formation of anthracycline-DNA adducts. *Anticancer Drug Des.* **2000**, *15*, 373–386.
3. Wang, A. H.; Gao, Y. G.; Liaw, Y. C.; Li, Y. K. Formaldehyde cross-links daunorubicin and DNA efficiently: HPLC and X-ray diffraction studies. *Biochemistry* **1991**, *30*, 3812–3815.
4. Sordet O.; Khan Q.A.; Kohn K.W.; Pommier Y. Apoptosis Induced by Topoisomerase Inhibitors. *Current Medicinal Chemistry - Anti-Cancer Agents* **2003**, *3*, 271–290.
5. Larsen, A. K.; Escargueil, A. E.; Skladanowski, A. Catalytic topoisomerase II inhibitors in cancer therapy. *Pharmacol. Ther.* **2003**, *99*, 167–181.
6. Phillips, D. R.; White, R. J.; Cullinane, C. DNA sequence-specific adducts of adriamycin and mitomycin C. *FEBS Lett.* **1989**, *246*, 233–240.
7. Swift, L. P.; Cutts, S. M.; Rephaeli, A.; Nudelman, A.; Phillips, D. R. Activation of adriamycin by the pH-dependent formaldehyde-releasing prodrug hexamethylenetetramine. *Mol. Cancer Ther.* **2003**, *2*, 189–198.
8. Fernández, C.; Szyperski, T.; Ono, A.; Iwai, H.; Tate, S.; Kainosho, M.; Wüthrich, K. NMR with 13C, 15N-doubly-labeled DNA: the Antennapedia homeodomain complex with a 14-mer DNA duplex. *J. Biomol. NMR* **1998**, *12*, 25–37.
9. Ulyanov, N. B.; Bauer, W. R.; James, T. L. High-resolution NMR structure of an AT-rich DNA sequence. *J. Biomol. NMR* **2002**, *22*, 265–280.
10. Bouaziz, S.; Kettani, A.; Patel, D. J. A K cation-induced conformational switch within a loop spanning segment of a DNA quadruplex containing G-G-G-C repeats. *Journal of Molecular Biology* **1998**, *282*, 637–652.

11. Post, G. C.; Barthel, B. L.; Burkhart, D. J.; Hagadorn, J. R.; Koch, T. H. Doxazolidine, a proposed active metabolite of doxorubicin that cross-links DNA. *J. Med. Chem.* **2005**, *48*, 7648–7657.
12. Rahman, A.; Carmichael, D.; Harris, M.; Roh, J. K. Comparative pharmacokinetics of free doxorubicin and doxorubicin entrapped in cardiolipin liposomes. *Cancer Res.* **1986**, *46*, 2295–2299.
13. Gmeiner, W. H.; Skradis, A.; Pon, R. T.; Liu, J. Cytotoxicity and in-vivo tolerance of FdUMP[10]: a novel pro-drug of the TS inhibitory nucleotide FdUMP. *Nucleosides Nucleotides* **1999**, *18*, 1729–1730.
14. Pardee, T. S.; Gomes, E.; Jennings-Gee, J.; Caudell, D.; Gmeiner, W. H. Unique dual targeting of thymidylate synthase and topoisomerase1 by FdUMP[10] results in high efficacy against AML and low toxicity. *Blood* **2012**, *119*, 3561–3570.
15. Phillips, D. R.; White, R. J.; Cullinane, C. DNA sequence-specific adducts of adriamycin and mitomycin C. *FEBS Lett.* **1989**, *246*, 233–240.
16. Min, K.; Jo, H.; Song, K.; Cho, M.; Chun, Y.-S.; Jon, S.; Kim, W. J.; Ban, C. Dual-aptamer-based delivery vehicle of doxorubicin to both PSMA (+) and PSMA (−) prostate cancers. *Biomaterials* **2011**, *32*, 2124–2132.
17. Ghosh, S.; Salsbury, F. R., Jr; Horita, D. A.; Gmeiner, W. H. Zn2+ selectively stabilizes FdU-substituted DNA through a unique major groove binding motif. *Nucleic Acids Res.* **2011**, *39*, 4490–4498.
18. Piotto, M.; Saudek, V.; Sklenár, V. Gradient-tailored excitation for single-quantum NMR spectroscopy of aqueous solutions. *J. Biomol. NMR* **1992**, *2*, 661–665.
19. Delaglio, F.; Grzesiek, S.; Vuister, G. W.; Zhu, G.; Pfeifer, J.; Bax, A. NMRPipe: a multidimensional spectral processing system based on UNIX pipes. *J. Biomol. NMR* **1995**, *6*, 277–293.
20. The PyMOL Molecular Graphics System, Version 1.5.0.4 Schrödinger, LLC.
21. Humphrey, W.; Dalke, A.; Schulten, K. VMD: visual molecular dynamics. *J Mol Graph* **1996**, *14*, 33–38, 27–28.
22. Stewart, J. J. P. Optimization of parameters for semiempirical methods V: Modification of NDDO approximations and application to 70 elements. *J Mol Model* **2007**, *13*, 1173–1213.
23. Gaussian 09, Revision **A.1**, Frisch, M. J.; Trucks, G. W.; Schlegel, H. B.; Scuseria, G. E.; Robb, M. A.; Cheeseman, J. R.; Scalmani, G.; Barone, V.; Mennucci, B.; Petersson, G. A.; Nakatsuji, H.; Caricato, M.; Li, X.; Hratchian, H. P.; Izmaylov, A. F.; Bloino, J.; Zheng, G.; Sonnenberg, J. L.; Hada, M.; Ehara, M.; Toyota, K.; Fukuda, R.; Hasegawa, J.; Ishida, M.; Nakajima, T.; Honda, Y.; Kitao, O.; Nakai, H.; Vreven, T.; Montgomery, Jr., J. A.; Peralta, J. E.; Ogliaro, F.; Bearpark, M.; Heyd, J. J.; Brothers, E.; Kudin, K. N.; Staroverov, V. N.; Kobayashi, R.; Normand, J.; Raghavachari, K.; Rendell, A.; Burant, J. C.; Iyengar, S. S.; Tomasi, J.; Cossi, M.; Rega, N.; Millam, J. M.; Klene, M.; Knox, J. E.; Cross, J. B.; Bakken, V.; Adamo, C.; Jaramillo, J.; Gomperts, R.; Stratmann, R. E.; Yazyev, O.; Austin, A. J.; Cammi, R.; Pomelli, C.; Ochterski, J. W.; Martin, R. L.; Morokuma, K.; Zakrzewski, V. G.; Voth, G. A.; Salvador, P.; Dannenberg, J. J.; Dapprich, S.; Daniels, A. D.; Farkas, Ö.; Foresman, J. B.; Ortiz, J. V.; Cioslowski, J.; Fox, D. J. Gaussian, Inc., Wallingford CT, 2009.

Appendix #4 – manuscript submitted for publication

Non-Covalent Assembly of Meso-tetra-4-Pyridyl Porphine with Single-Stranded DNA to Form Nano-sized Complexes with pH-Dependent DNA Release and Anti-Tumor Activity

Supratim Ghosh, PhD[†,‡], Kamil B. Ucer, PhD[§], Ralph D'Agostino, PhD[ℨ], Ken Grant, BS[≠], Joseph Sirintrapun, MD[≠], Michael Thomas, PhD[#], Roy Hantgan, PhD[#], Manish Bharadwaj, PhD[υ], William H. Gmeiner, PhD, MBA[†,‡,ℨ,*]

[†]Program in Molecular Genetics, [‡]Department of Cancer Biology, [≠]Department of Pathology [#]Department of Biochemistry, [υ]Department of Genrontology, [ℨ]Comprehensive Cancer Center Wake Forest School of Medicine, Winston-Salem NC 27157
[§]Department of Physics, Wake Forest University, Winston-Salem, NC 27106

Short Title: Porphyrin:DNA nanoparticle for cancer therapy

***Name and Address correspondence to this author:**
William H. Gmeiner
Department of Cancer Biology, Wake Forest School of Medicine
Winston-Salem, NC 27157
Phone: (336) 716-6216; Fax: (336) 716-0255; Email: bgmeiner@wakehealth.edu

Funding Resources: This work was supported by DOD PCRP 093606 (WHG) and NIH-NCI P30CA012197 (WHG).

Abstract Word count: 143

Complete Manuscript Word Count: 4826

ABSTRACT:

DNA and porphyrins are important materials for anti-cancer treatment. The present studies demonstrate single-stranded DNA (ssDNA) assembles with meso-tetra-4-pyridyl porphine (MTP) forming porphyrin:DNA nano-complexes (PDN) that are stable in aqueous solution under physiologically relevant conditions and undergo pH-dependent

dissociation with DNA release in endosomes after internalization into cancer cells. PDN formation is DNA-dependent with the ratio of porphyrin:DNA being approximately two DNA nucleobases per porphyrin. PDN produce reactive oxygen species (ROS) in a light-dependent manner under conditions that favor nano-complex dissociation or in the presence of hydrophobic solvents. PDN induce light-dependent cytotoxicity *in vitro* and anti-tumor activity towards bladder cancer xenografts *in vivo*. Light-dependent, PDN-mediated cell death results from ROS-mediated localized membrane damage with mass spectrometry confirming the generation of the lipid peroxidation products 9- and 13-hydroxy octadecanoic acid. Our results demonstrate that PDN have properties useful for therapeutic applications, including cancer treatment.

Key Words: Multi-modality Nanoparticle, Cancer Therapy, Photodynamic Therapy, Porphyrin:DNA assembly.

BACKGROUND:

Porphyrins are a group of compounds containing the porphin ring structure that are important in biology and medicine and that have recently been studied for their propensity to form nanomaterials,[1, 2] including nanotubes[3] through non-covalent chemistry. The principal driving force for porphyrin self-assembly is hydrophobic interactions[4] resulting in vertical stacking of porphyrins in aqueous solutions in a pH-dependent manner.[5, 6] Previous studies demonstrating nanoparticle assembly of

porphyrins were conducted in pure water and self-assembly was optimal at acidic pH limiting potential biological applications.[5, 6] Porphyrin assembly has been shown to be modulated by biological molecules, such as poly-glutamic acid,[7] however these complexes also have limited stability under biologically relevant conditions. The preparation of porphyrin-containing nanostructures that are stable under biologically relevant conditions, but that dissociate in a predicable manner could be useful for drug delivery, photodynamic therapy (PDT),[8-12] and other biologically relevant processes.[13]

The present studies focus on developing porphyrin:DNA nanoparticles (PDN) that are stable under physiological conditions of pH, salt, and temperature and that have potential use for PDT as well as in nucleic acid delivery. In principle, hydrophobic stacking and hydrogen bonding interactions between appropriately modified porphyrins and DNA (or RNA) nucleobases could provide an additional interaction complementary to porphyrin aggregation potentially resulting in production of porphyrin:DNA nanoparticles (PDN) that have both the light-mediated cell killing properties of porphyrin photosensitizers (PS) and the capacity to deliver a nucleic acid payload with therapeutic utility. Our studies utilize meso-tetra-4-pyridyl porphin (MTP) interacting with the single-stranded DNA (ssDNA) $(GT)_{20}$. In the absence of DNA, MTP forms amorphous aggregates in aqueous solution under physiological conditions, although acidification of the solution (< pH 5.5) dissociates the aggregates and re-generates non-complexed porphyrin. The pyridyl groups of MTP have the potential to base stack and/or form hydrogen bonds with nucleobases of DNA at physiological pH and the phosphodiester backbone of DNA may confer aqueous solubility to the complex. We demonstrate that unlike previous poprhyrin:DNA complexes,[14-18] the PDN developed with this approach

form discrete porphyrin:DNA nanoparticles that are of the appropriate size for drug-delivery applications via the enhanced permeability and retention (EPR) effect[19, 20] and that readily dissociate upon cell internalization to deliver a therapeutic payload.

The PDN prepared by self-assembly of MTP and ssDNA have the potential to be highly effective agents for cancer treatment. We demonstrate that PDN are capable of exerting light-dependent cytotoxicity towards bladder cancer cells both in tissue culture models and *in vivo*. The light-dependent cytotoxicity of PDN occurs with generation of the lipid oxidation products 9- and 13-hydroxy octadecanoic acid (HODE) and with damage to the integrity of the plasma membrane consistent with generation of singlet oxygen via a type II photochemical reaction.[21] PDN initially associate with the plasma membrane and are internalized into endocytic vesicles where free DNA and porphyrin are released recovering the functionality of the constituent materials leaving no extraneous carrier that may impart systemic toxicities. Importantly, localized PDN-treatment combined with light activation significantly reduced tumor volumes *in vivo*.

METHODS

Preparation of porphyrin:DNA nanoparticles. Meso-tetra-4-pyridyl porphine (MTP; ~0.25 mg - Frontier Scientific) was suspended in 5 mL 20mM Phosphate Buffer (pH-7.4) containing 5 nmol (0.025mg/mL) $d(GT)_{20}$ and sonicated in a bath sonicator for 1.5hrs with temperature maintained at 5-7 ^{o}C. A second addition of MTP (~0.25 mg) was followed by an additional 1 h sonication, followed by addition of 5 nmol DNA and further sonication for 1 hour. The mixture was then centrifuged and the resulting brownish-yellow aqueous suspension was used for subsequent studies. The porphyrin:DNA ratio

for PDN (~19:1) was calculated by acid dissolution of the nanoparticle followed by spectrophotometric determination.

Spectroscopic Characterization of PDN. UV-Vis spectra were collected under ambient conditions using a DU800 UV-Vis spectrophotometer (Beckman Coulter). Fluorescence spectra were acquired using a Perkin-Elmer-F1000 fluorometer with excitation at 420nm and emission scanned over the range 550-900 nm. Transmission electron microscopy (TEM) images of PDN were acquired under ambient conditions using a FEI Thcnai-Spirit TEM. TEM images were analyzed and the distribution of PDN length and diameter were determined using Matlab software. Dynamic light scattering (DLS) was performed under ambient conditions using a Malvern Zetasizer nano series ZEN-1600 in particle size and molecular weight measurement mode. Each sample was read for 60 sec using a 442.0 Kcps count rate. Data were analyzed using Malvern software.

Tissue Culture Cytotoxicity and Apoptosis Assays. Human bladder cancer cells (ATCC 5637) were cultured in complete media (RPMI + 10%FBS). The cells were then treated with complete media containing nanoparticle at final concentrations of 0, 1, 2, 5 μg/mL followed by incubation overnight then washed with PBS. One of two plates was then exposed to 420nm blue light (Trophy Skin Blue MD) at a power density of 2.3 μW /cm^2 for 10 min followed by incubation for 24 hours. Cell viability was assessed using the CellTiter 96 Proliferation Assay reagent (Promega) following the manufacturer's instructions. Apoptosis assays using the Caspase Glo 3/7 assay (Promega) were conducted using similar procedures except PDN concentration was evaluated at 0 or 2 μg/mL. Luminescence was measured using GENios (TECAN) microplate reader. All

experiments were done in triplicate. Each set of data (net absorbance) were expressed as a percentage, considering the no treatment group as 100%.

Light-Dependent Membrane Damage by PDN. Localized membrane damage of PDN upon blue light irradiation was evaluated using confocal microscopy to detect calcein-AM, a cytoplasm-localizing fluorescent dye. Cells were treated with complete media containing PDN (0 or 2 μg/mL), incubated overnight at 37 ^{o}C, washed with PBS followed by addition of Calcein-AM (Invitrogen) at final concentration 2.5 μM, and incubated for 15 min at 37 ^{o}C. One of the two chamber slides was then exposed to 420 nm blue light for 10 min. Cells were imaged using a Zeiss Axiovert LSM-510 microscope. PDN were excited using the 633 nm laser with emission collected with the 650 nm long-pass filter set. Calcein-AM was excited using the 488 nm argon laser with emission collected with 505 – 530 nm bandpass filter set. DIC images of cells were collected in a separate channel for overlay.

Light-Dependent Membrane Lipid Peroxidation by PDN. Membrane lipid peroxidation upon blue light irradiation of cancer cells treated with PDN was evaluated using confocal microscopy detecting a membrane localizable fluorescent dye (C11-Bodipy). Microscopy was performed as described for Calcein-AM detection.

Detection of Light-Dependent Membrane Damage by PDN. PDN-mediated membrane damage upon blue light irradiation was detected by Transmission Election Microscopy (TEM). Cell culture and PDN treatment, including blue light irradiation, was performed in 6-well white clear bottom plates (Costar) following the same procedure as for the in vitro cytotoxicity assay except the PDN concentration was 0 or 2 μg/mL. Cells were fixed with 2.5% glutaraldehyde and treated with 2% osmium tetroxide, then

dehydrated gradually followed by embedding in the resin and sectioning for TEM investigation.

Antitumor activity of PDN. All animal experiments were performed in accordance with protocols approved by the Wake Forest School of Medicine Animal Care and Use Committee. Six week old female nude mice were ordered from NCI. Each of 10 mice was injected with 100 μL of 250 μg/mL PDN suspension in one flank and 100 μL saline in the other flank. Approximately 12 h later, tumors on both flanks of 6 mice were irradiated with a blue beam of 420nm for 3 min. The source laser for these studies was a Mira 900 (Coherent Inc., Santa Clara, CA), a mode-locked femtosecond Ti:Sapphire laser. The pulses were approximately 90 femtoseconds at a wavelength of 840 nm with an average power of 600 mW. The beam was transmitted directly into the tumor using a multimode optical fiber (SFS105/125Y, Thorlabs Inc., Newton, NJ). The output power at the final end of the fiber was 100 mW. The remaining four mice were treated identically but were not exposed to the laser. The laser irradiation was performed every 5th day for a total of five doses. Tumor sizes were measured using calipers and tumor volumes were calculated using the formula $xy^2\pi/6$ (where x and y are the long and short diameters of the tumor, respectively). The tumors were analyzed as four independent groups: i) no treatment; ii) light-only; iii) PDN-only; iv) PDN + light. Relative tumor volumes (V/V_o) were graphed vs. time (where V is the present tumor volume and V_o was the tumor volume when treatment started). Repeated measures mixed models were fit to compare tumor volumes between groups. In these models, animals were treated as random effects and group (four-levels) and time (days) were treated as fixed-effects. The group-by-time interaction was examined to determine whether the rate of

change in tumor volume differed over time among the four groups. All statistical analyses were performed using SAS 9.1.

Histopathological Analysis of Tumor Tissue. At the conclusion of the study animals were sacrificed and tumors were excised and placed in 4% paraformaldehyde solution overnight at ambient temperature. The following day, tumors were embedded in molten paraffin and thin sections were prepared from different layers of tumors and placed on glass slides followed by H&E staining.

RESULTS

Biophysical Properties of Porphyrin:DNA Nanoparticles. Meso-tetra-4-pyridyl porphine (MTP – Figure 1A) is soluble in aqueous solution only at acidic pH (< 5.5) and forms aggregates in solution near physiological pH. Sonication of MTP in the presence of single-stranded DNA at pH 7.4, however, permitted recovery of discrete nano-sized particles composed of both porphyrin and DNA (porphyrin:DNA nanoparticles – PDN; Figure 1B). Production of nanoparticles (Figure S1, Supporting Information) was DNA-dependent and the ratio of porphyrin to DNA ($d(GT)_{20}$) was determined to be ~19:1 (mol/mol) or about two DNA nucleobases per MTP based upon the UV absorbances calculated from the acid-dissolved nanoparticles (Table S1 and Figure S2, Supporting Information). The size and shape of the PDN were investigated using transmission electron microscopy (TEM - Figure 1C) and the hydrodynamic properties of PDN were

investigated using dynamic light scattering (DLS - Figure 1D). TEM images revealed irregular shaped particles with average length and diameter ~60 nm (Figure S3, Supporting Information) while DLS revealed PDN in aqueous solution had an average hydrodynamic radius of ~295 nm (Figure 1D).

PDN were characterized by UV-Vis, fluorescence, and Raman spectroscopies to determine to what extent the context of the PDN complex altered the electronic properties of the constituent porphyrin and DNA. UV-Vis spectra for PDN revealed the absorbance at 260 nm from the DNA was little changed relative to free DNA while the Soret (S0 -> S2) band[22] was slightly red-shifted and broadened for PDN relative to MTP (Figure 2A). The Q band (S0 -> S1)[23] at 535 nm was also enhanced and sharpened for the PDN relative to the free porphyrin. Fluorescence spectra for PDN with excitation at 415 nm showed that the emission maxima at 660 and 725 nm for the MTP monomer were substantially quenched for PDN with emission maxima reduced ~25-fold (Figure 2B). Raman spectra (457.9 absorption; Figure 2C) revealed two sharp peaks at 1360 and 1555 cm^{-1} for PDN similar to resonances assigned previously to $(\nu_{(X\beta-X\beta)} + (_X\beta-H))$ and $(\nu_{(X\alpha-N)} + \delta_{(X\beta-H)})$ for tetrasulfonated tetraphenyl porphyrin (TSSP) upon electrode binding,[24] consistent with surface-enhancement of Raman spectra for MTP in the context of PDN. Together, the spectroscopic properties reveal an altered electronic structure for MTP in the context of PDN that is consistent with $\pi-\pi$ stacking of porphyrins with DNA nucleobases contributing significantly to PDN assembly.

pH-Dependent PDN Dissociation and DNA Release. The stability of PDN as a function of pH and solvent hydrophobicity was investigated to gain insight into the nature of forces promoting complex stability (Figure 3). PDN stability was pH-

dependent in aqueous buffers with significant enhancement in both A_{260} and A_{415} absorbance signifying both DNA and porphyrin release from PDN upon acidification to pH 5.1, the pK_A for pyridyl nitrogen protonation, or pH 11.4, the pK_A for imino hydrogen deprotonation (Figure 3A). Fluorescence intensity for MTP was also enhanced upon acidification consistent with porphyrin release (Figure 3D).

While the pH-dependence of PDN dissociation is consistent with either disruption of hydrogen bonding or hydrophobic base stacking between DNA and MTP promoting complex assembly, the dissociation of PDN was also favored by increasing the hydrophobicity of the solvent system by acetonitrile addition (Figure 3B, 3C) and the pH-dependence of dissociation was attenuated in hydrophobic solvent systems consistent with hydrophobic base stacking between DNA nucleobases and pyridyl side chains of MTP being important for complex stability. Thus, the data are consistent with $\pi-\pi$ stacking between DNA nucleobases and pyridyl side chains of MTP significantly contributing to PDN stability.

The pH-dependence of PDN dissociation *in vitro* caused us to investigate to what extent PDN dissociate in acidic environments *in vivo*. Increased acidity is associated with the tumor microenvironment raising the possibility that PDN may dissociate selectively in tumor tissue. Endosomes are also acidic and thus PDN may dissociate upon cellular internalization due to pH-dependent effects or as a consequence of interactions with the hydrophobic lipid membrane. We performed confocal microscopy experiments with fluorescently (6-FAM) labeled DNA and evaluated PDN dissociation and DNA release upon cellular internalization (Figure 3E). Confocal images revealed DNA release and also detection of fluorescence from free porphyrin following cellular

internalization. The focal, punctate localization of fluorescence (Figure 3E) is consistent with PDN dissociation and DNA release in endosomes.

***In vitro* Heating and ROS Production of PDN**. Porphyrins are widely used for PDT[25] in which absorbed light is used for production of cytotoxic ROS. The UV-Vis spectra for PDN indicated UV/Vis absorption was attenuated relative to the same concentration of free MTP (~2-fold) (Figure 2A) while fluorescence for the PDN complex is quenched relative to MTP (Figure 2B) consistent with absorbed light being dissipated as heat and/or used for ROS production. The time- and concentration-dependence for heating of aqueous solutions of PDN was evaluated to determine whether temperature increases of a magnitude required for cell-killing could be induced under biologically relevant conditions (Figure S4, Supporting Information). PDN are not efficient transducers of heat although measurable temperature increases were detected upon photo-stimulation.

We also evaluated the light-dependent production of ROS by PDN using the fluorescent dye C11-bodipy that undergoes a change in absorbance from red to green upon oxidation by ROS. Evidence for C11-bodipy oxidation mediated by PDN occurred selectively in a light-dependent manner only in solvent systems that favored PDN dissociation such as the presence of acetonitrile (Figure 5B) and/or at acidic pH. The results are consistent with intact PDN not mediating light-dependent ROS production however, under conditions that favor PDN dissociation light-dependent ROS production occurred.

Light-Dependent Cytotoxicity of PDN. The cytotoxicity of PDN towards human bladder cancer cells was evaluated to determine to what extent these nano-sized

complexes are cytotoxic towards malignant cells in a light-dependent manner (Figure 4 and Figures S5-S8, Supporting Information). ROS resulting from PDN dissociation in endosomes or upon interacting with the plasma membrane could, upon light stimulation, result in lipid peroxidation with subsequent loss of membrane integrity and cell death (Figure 4A). Cytotoxicity assays demonstrated PDN are cytotoxic to bladder cancer cells in a light-dependent manner (Figure 4B). Interestingly, the light-dependent cytotoxicity of PDN towards bladder cancer cells is relatively independent of PDN concentration consistent with a threshold level of membrane damage inducing cell death. The light-dependent cytotoxicity of PDN was accompanied by only a slight increase in apoptosis (Figure 4C), with little DNA damage (Figure S9, Supporting Information) and no effect of z-VAD rescue (Figure S9, Supporting Information) consistent with cell death being predominantly non-apoptotic.

To gain further insight into the nature of cell death, bladder cancer cells were pre-treated with the cell impermeable dye calcein-AM and the effects of PDN and light on calcein retention were investigated. Treatment with PDN and light resulted in dye efflux for nearly all cells (Figure 4D) while treatment with PDN- or light-only did not stimulate dye efflux (Figure 4D). The results indicate cell death is accompanied by a loss of membrane integrity. Interestingly, the free radical scavenger N-acetyl cysteine (NAC) did not rescue cells from the light-mediated cytotoxicity of PDN (Figure S7, Supporting Information). The results are consistent with PDN exerting localized cell damage that is not affected by the REDOX state of the cell.

Cell Death is Mediated by Localized Oxidation of Membrane Lipids. The light-dependent cytotoxic mechanism of PDN was further investigated using confocal

microscopy, TEM, and mass spectrometry to determine if physical damage to the plasma membrane and endosomal compartments were important for PDN-mediated cell death (Figure 5 and Figure S8, Supporting Information). The nature of the observed membrane damage was investigated using the fluorescent dye Bodipy[26] to visualize the occurrence of oxidized lipids in the plasma membrane of bladder cancer cells treated with PDN and light (Figure 5A). PDN convert Bodipy to the oxidized form in a light-dependent manner only in solution conditions that favor PDN dissociation, such as in hydrophobic solvent systems (Figure 5B). The results demonstrate that treatment of bladder cancer cells with PDN and light, but not light-only, resulted in increased levels of oxidized lipids, as well as detection of free porphyrin (Figure 5A). TEM images revealed PDN were associated with the plasma membrane and internalized, likely in endosomes, and that substantial membrane damage and vacuole formation was observed proximal to nanoparticles in a light-dependent manner (Figure 5D). Confocal microscopy studies demonstrated that non-complexed porphyrin and DNA were released from PDN upon cellular internalization (Figure 5A) thus photo-mediated damage may result from non-complexed porphyrin released from PDN after cell internalization. The presence of oxidized lipids in the plasma membrane was investigated further using mass spectrometry. Mass spectrometry confirmed that elevated levels of 9-HODE and 13-HODE, products resulting from lipid peroxidation,[27] occurred selectively in cells treated with PDN and light (Figure 5C). Together, these results indicate cell death following treatment with PDN and light occurred from localized membrane damage leading to a loss of plasma membrane integrity.

PDN Display Light-Dependent Antitumor Activity *in vivo*. The light-dependent cytotoxicity of PDN towards bladder cancer cells in tissue culture invites the question of whether PDN can be used for light-dependent reduction or eradication of tumors *in vivo*. To address this question, we formed xenograft tumors bilaterally on the flanks of nude mice (Figure 6A and Figure S10, Supporting Information). Initial tumor volumes were ~75 mm^3 and there was no difference among the treatment groups at baseline. Tumors were treated by direct injection of either PDN or a saline solution. The tumor groups were further divided into light-treated and mock-treated groups to create four groups: i) no treatment; ii) light-only; iii) PDN-only; iv) PDN + light. Light treatment was achieved by inserting a fiber-optic cable into the tumor followed by treatment with 420 nm laser light for 3 min. Tumors that were not light-treated underwent a similar number of identical procedures introducing the fiber-optic cable without light exposure. The time-dependence of tumor growth and regression is shown in Figure 6B. Beginning around day 20 tumors treated with either light or PDN + light displayed tumor regression while the untreated tumors began to display more rapid growth. Tumors treated with PDN and light displayed significant tumor regression that was superior to no treatment or treatment with PDN-only beginning on day 20 and achieving statistical significance at day 30 and persisting until the conclusion of the study ($p < 0.05$). Tumor regression following treatment with PDN and light was significantly greater than for light-only beginning on day 40 and achieving statistical significance at day 49 and persisting until completion of the study ($p < 0.05$). The results demonstrate that PDN display light-dependent anti-tumor activity *in vivo.*

Histopathological Analysis of Tumor Tissue Following Treatment with PDN. At the conclusion of the *in vivo* study, tumor tissue was removed from sacrificed mice and sectioned for morphologic evaluation. In all study groups, sections showed subcutaneous tumoral deposits comprised of urothelial carcinoma with high-grade cytology and partial keratinization. Tumor tissue from mice in the control group that received neither nanoparticle nor light showed only subcutaneous tumoral deposits. Polarization revealed no polarizable nanoparticles (Figure 6C and Figure S12, Supplementary Information) and there was minimal fibrosis, chronic inflammation, or reparative changes. Tumor tissue from mice treated with light-only revealed similar features as those mice in the control group. For mice in both the PDN-only and the PDN/light groups, polarization revealed the presence of nanoparticles confirming the persistence of PDN at the site of injection for several weeks and demonstrating light-treatment does not affect PDN stability. (Figure 6C and Figure S12, Supplementary Information). For the PDN-only group, tumor was absent in areas which nanoparticle was present demonstrating PDN having a native mild tumor abortive effect even in the absence of light. For the PDN/light group, tumor was also absent in the areas which nanoparticle was present but there was marked fibrosis, chronic inflammation, and reparative changes. This supports a potent tumor abortive effect likely accentuated by light excitation; a result which already accentuates the native anti-tumor activity of PDN. Some areas of tumor not displaying polarizable nanoparticles, however, showed tumor re-growth consistent with incomplete penetration of nanoparticles. Another advantage appears that the range of anti-tumor activity is confined to zones around PDN deposition, allowing for precise margins with this therapeutic approach.

DISCUSSION

The present studies demonstrate that discrete nano-sized particles can be obtained from self-assembly of MTP and DNA under controlled conditions. Discrete nanoparticles do not form for MTP in the absence of DNA indicating DNA:porphyrin interactions are critical for PDN assembly. The ratio of porphyrin to DNA in PDN (~19:1) (mol/mol) is consistent with two nucleobases from each DNA 40-mer interacting with each porphyrin. Thus, approximately half the pyridyl side chains in each MTP (Figure 1A) may be engaged in interactions with DNA nucleobases (Figure 1B). The spectroscopic results are consistent with π–π stacking between pyridyl side chains and DNA nucleobases as being a principal driving force for nanoparticle assembly. PDN display quenching of porphyrin fluorescence and increased intensity and sharpness for Raman spectra similar to that observed upon surface-enhancement for free porphyrins. PDN dissociation is favored at pH that favor pyridine protonation or imino hydrogen deprotonation consistent with either disruption of hydrogen bonding between DNA and porphyrin or introduction of charge disfavoring π–π stacking between DNA and porphyrin. PDN dissociation was also favored by increasing the hydrophobicity of the solvent system consistent with π–π stacking being a significant force. Further, PDN dissociation was relatively pH-independent in hydrophobic solvent systems. Thus PDN stability appears to result from π–π stacking between PDN and DNA with aqueous solubility conferred by the phosphodiester backbone of DNA.

We have demonstrated that PDN cause cell death predominantly via localized membrane damage resulting in necrotic cell death. While conventional photosensitizers can induce membrane damage upon light stimulation, a variety of other cellular

organelles, including the mitochondria,[28] are also potential sites for PDT-induced damage. Our studies demonstrate PDN localize to the plasma membrane and also undergo internalization via endocytosis. Upon internalization into endocytic vesicles the fluorescence of FAM-labeled DNA and porphyrin are readily apparent (Figure 3E) consistent with PDN dissociation in the hydrophobic environment of cell membranes or vesicles. Photo-mediated damage mediated by released porphyrin results in loss of plasma membrane integrity and vacuole formation (Figure 5) that is accompanied by lipid oxidation and specifically generation of the oxidized fatty acids 9-HODE and 13-HODE (Figure 5C).

Importantly, PDN/light treatment of bladder cancer xenografts resulted in significant reduction in tumor volumes *in vivo* (Figures 6A,B). Histopathological analysis of tumor tissue revealed PDN/light displayed strong tumorpathic properties and elicited inflammatory and reparative changes associated with an immune response (Figure 6C and Figure S11, Supporting Information). No tumor tissue was identified in regions where PDN were localized indicating PDN/light treatment exerts powerful anti-tumor effects with very tight margins. These results indicate PDN/light may be highly effective for cancer treatment in humans.

These studies demonstrate the potential of PDN for cancer treatment, however PDN are multi-modality nanoparticles and DNA-release may contribute to the overall therapeutic response. PDN readily dissociate upon cellular internalization as a consequence of the hydrophobic environment in cell membranes and the acidic pH in the tumor microenvironment or in endocytic vesicles releasing DNA and free porphyrin (Figure 4d). Dissociated nucleic acid may exert additional anti-tumor activity increasing

the activity of PDN and providing a therapeutic advantage not realizable using conventional photosensitizers or nanoparticles that do not include a DNA component. Importantly, PDN are biocompatible and elicited no apparent morbidity upon *in vivo* administration.

SUPPLEMENTARY INFORMATION

A description of PDN preparation, analysis of porphyrin:DNA stoichiometry, analysis of PDN size distribution, representative plots of sample heating, a photograph of the experimental set-up and results of additional *in vitro* and *in vivo* experiments are included.

ACKNOWLEDGMENT

The authors acknowledge Dr. Baidyanath Saha for helping with TEM image analysis; Chris Stuart for helping with *in vivo* experiments; Michael Samuel for helping with mass-spectrometry experiment; Dr. David A. Horita for helping with nanoparticle model building; and WFU Department of Physics for use of laser facilities.

REFERENCES

1. X. Gong, T. Milic, C. Xu, J. D. Batteas and C. M. Drain, **Preparation and characterization of porphyrin nanoparticles**. *J Am Chem Soc*. 2002;124:14290-1

2. X. L. Liang, X. D. Li, X. L. Yue and Z. F. Dai, **Conjugation of Porphyrin to Nanohybrid Cerasomes for Photodynamic Diagnosis and Therapy of Cancer**. *Angewandte Chemie-International Edition*. 2011;50:11622-11627

3. Z. C. Wang, C. J. Medforth and J. A. Shelnutt, **Porphyrin nanotubes by ionic self-assembly**. *Journal of the American Chemical Society*. 2004;126:15954-15955

4. C. M. Drain, G. Smeureanu, S. Patel, X. C. Gong, J. Garno and J. Arijeloye, **Porphyrin nanoparticles as supramolecular systems**. *New Journal of Chemistry*. 2006;30:1834-1843

5. M. De Napoli, S. Nardis, R. Paolesse, M. G. Vicente, R. Lauceri and R. Purrello, **Hierarchical porphyrin self-assembly in aqueous solution**. *J Am Chem Soc*. 2004;126:5934-5

6. R. Lauceri, M. De Napoli, A. Mammana, S. Nardis, A. Romeo and R. Purrello, **Hierarchical self-assembly of water-soluble porphyrins**. *Synthetic Metals*. 2004;147:49-55

7. E. Bellacchio, R. Lauceri, S. Gurrieri, L. M. Scolaro, A. Romeo and R. Purrello, **Template-imprinted chiral porphyrin aggregates**. *Journal of the American Chemical Society*. 1998;120:12353-12354

8. S. Anand, B. J. Ortel, S. P. Pereira, T. Hasan and E. V. Maytin, **Biomodulatory approaches to photodynamic therapy for solid tumors**. *Cancer Lett*. 2012;326:8-16

9. M. L. Davila, **Photodynamic therapy**. *Gastrointest Endosc Clin N Am*. 2011;21:67-79

10. M. Ethirajan, Y. Chen, P. Joshi and R. K. Pandey, **The role of porphyrin chemistry in tumor imaging and photodynamic therapy**. *Chem Soc Rev*. 2011;40:340-62

11. L. B. Josefsen and R. W. Boyle, **Unique diagnostic and therapeutic roles of porphyrins and phthalocyanines in photodynamic therapy, imaging and theranostics**. *Theranostics*. 2012;2:916-66

12. A. E. O'Connor, W. M. Gallagher and A. T. Byrne, **Porphyrin and nonporphyrin photosensitizers in oncology: preclinical and clinical advances in photodynamic therapy**. *Photochem Photobiol*. 2009;85:1053-74

13. S. P. Walton, M. Wu, J. A. Gredell and C. Chan, **Designing highly active siRNAs for therapeutic applications**. *Febs J*. 2010;277:4806-13

14. G. Ananyan, A. Avetisyan, L. Aloyan and Y. Dalyan, **The stability of DNA-porphyrin complexes in the presence of Mn(II) ions**. *Biophys Chem*. 2011;156:96-101

15. M. Bennett, A. Krah, F. Wien, E. Garman, R. Mckenna, M. Sanderson, et al., **A DNA-porphyrin minor-groove complex at atomic resolution: The structural consequences of porphyrin ruffling**. *Proceedings of the National Academy of Sciences of the United States of America*. 2000;97:9476-9481

16. A. D'Urso, A. Mammana, M. Balaz, A. E. Holmes, N. Berova, R. Lauceri, et al., **Interactions of a tetraanionic porphyrin with DNA: from a Z-DNA sensor to a versatile supramolecular device**. *J Am Chem Soc*. 2009;131:2046-7

17. N. E. Geacintov, V. Ibanez, M. Rougee and R. V. Bensasson, **Orientation and Linear Dichroism Characteristics of Porphyrin DNA Complexes**. *Biochemistry*. 1987;26:3087-3092

18. L. A. Lipscomb, F. X. Zhou, S. R. Presnell, R. J. Woo, M. E. Peek, R. R. Plaskon, et al., **Structure of a DNA - Porphyrin complex**. *Biochemistry*. 1996;35:2818-2823

19. R. K. Jain and T. Stylianopoulos, **Delivering nanomedicine to solid tumors**. *Nat Rev Clin Oncol*. 2012;7:653-64

20. H. Maeda, **Macromolecular therapeutics in cancer treatment: The EPR effect and beyond**. *J Control Release*. 2012

21. K. Plaetzer, B. Krammer, J. Berlanda, F. Berr and T. Kiesslich, **Photophysics and photochemistry of photodynamic therapy: fundamental aspects**. *Lasers Med Sci*. 2009;24:259-68

22. V. N. Nemykin and R. G. Hadt, **Interpretation of the UV-vis spectra of the meso(ferrocenyl)-containing porphyrins using a TDDFT approach: is Gouterman's classic four-orbital model still in play?** *J Phys Chem A*. 2012;114:12062-6

23. Z. H. Lan M, Yuan H, Jiang C, Zuo S, Jiang Y **Absorption and EPR spectra of some porphyrins and metalloporphyrins**. *Dyes and Pigments*. 2007;74:357-362

24. T. Cotton, Schultz, SG, van Duyne, RP, **Surface-enhanced resonance Raman scattering from water-soluble adsorbed on a silver electrode**. *J. Am. Chem. Soc.* 1982;104:6528-6532

25. R. R. Allison and C. H. Sibata, **Oncologic photodynamic therapy photosensitizers: a clinical review**. *Photodiagnosis Photodyn Ther*. 2010;7:61-75

26. G. P. Drummen, L. C. van Liebergen, J. A. Op den Kamp and J. A. Post, **C11-BODIPY(581/591), an oxidation-sensitive fluorescent lipid peroxidation probe: (micro)spectroscopic characterization and validation of methodology**. *Free Radic Biol Med*. 2002;33:473-90

27. A. Catala, **Lipid peroxidation of membrane phospholipids generates hydroxy-alkenals and oxidized phospholipids active in physiological and/or pathological conditions**. *Chem Phys Lipids*. 2009;157:1-11

28. V. Rapozzi, M. Miculan and L. E. Xodo, **Evidence that photoactivated pheophorbide a causes in human cancer cells a photodynamic effect involving lipid peroxidation**. *Cancer Biol Ther*. 2009;8:1318-27

FIGURE LEGENDS

Figure 1. Discrete porphyrin:DNA nanoparticles (PDN) form upon sonication of MTP porphyrin with ssDNA. (A) Structure of the MTP porphyrin used for these studies; (B) Molecular model of PDN nano-complex showing both porphyrin-porphyrin and porphyrin:DNA interactions; (C) TEM image of PDN nanoparticles; (D) DLS analysis of PDN hydrodynamic radius distribution.

Figure 2. Spectroscopic characterization of PDN reveals the physical properties of the porphyrin are altered in the PDN complex. (A) Absorbance spectra for PDN (blue), MTP monomer (green), DNA (red), and phosphate buffer (black); (B) Fluorescence spectra for MTP monomer (green), PDN (blue), DNA (black), and 5% acetic acid (magenta); (C) Raman spectrum for PDN.

Figure 3. PDN-disassembly as a function of pH and solvent hydrophobicity. (A-B) Representative graphs of UV-Vis absorbance for PDN in aqueous solution at (A) pH 5.1, 7.4, 11.4 showing increase in 260 nm band (characteristic of DNA) and 415 nm (characteristic of MTP) indicating disassembly of the PDN complex; (B) at pH 7.4 in

aqueous buffer with increasing acetonitrile composition (25 – 75%) showing increase in PDN dissociation with increasing solvent hydrophobicity. (C-D) Representative graphs of fluorescence spectra (excitation – 415 nm) for PDN at pH-7.4 with increasing acetonitrile concentration (25 – 75%) showing an increase in the 660 and 720 nm MTP fluorescence consistent with PDN dissociation with increasing solvent hydrophobicity and (D) decreased solvent pH. (E) Confocal microscopy images evaluating PDN dissociation and DNA release. PDN were prepared with fluorescently-labeled (6-FAM) DNA: (left) porphyrin fluorescence; (middle) DNA fluorescence; (right) overlay of porphyrin and DNA fluorescence. Fluorescence is localized in a punctate pattern consistent with PDN dissociation and DNA release in endosomes.

Figure 4. PDN are cytotoxic to bladder cancer cells via localized damage to the plasma membrane as a consequence of light-activated oxidation of membrane lipids. (A) Depiction of a cancer cell with PDN localized to the plasma membrane and with light ($h\nu$) irradiation; inset displays an enlargement of the lipid bilayer of the plasma membrane with a PDN complex internalized in the membrane and shows further structures for the 9-HODE and 13-HODE lipid peroxidation products detected by mass spectrometry following PDN/light treatment. The green efflux reflects loss of calcein-AM dye resulting from membrane damage; (B) Cytotoxicity assay results showing PDN/light reduces bladder cancer viability; (C) Apoptosis assay results showing PDN-mediated cell death is predominantly non-apoptotic; (D) Confocal microscopy images displaying overlay of calcein-AM (green) fluorescence on DIC images for bladder cancer cells

following treatment with (left – right) no-treatment, light-only, PDN-only, PDN/light. Treatment with PDN/light resulted in efflux of calcein-AM.

Figure 5. PDN/Light treatment results in oxidation of plasma membrane lipids and localized membrane damage. (A) Confocal microscopy images displaying free porphyrin (left – magenta), oxidized membrane lipids detected with Bodipy (center – green), and non-oxidized membrane lipids detected with Bodipy (right-red). The top panels are from bladder cancer cells treated with PDN/light while the bottom panels are from light-only cells. (B) Representative fluorescence spectrum of dye c11 bodipy in presence of PDN+Light (red); PDN (green); Light only (blue) and control (black) with excitation 480 nm in pH-7.4 in 75% ACN + 25% aqueous solution mixture. (C) Quantification of lipid peroxidation products 9-HODE and 13-HODE from plasma membrane preparation from bladder cancer cells treated with PDN/light, light-only, PDN-only, and no treatment. (D) TEM images of bladder cancer cells treated with PDN/light (top-left), PDN-only (top-right), light-only (bottom-left), and no-treatment (bottom-right).

Figure 6. PDN/Light treatment displays significant anti-tumor activity *in vivo*. (A) Representative tumors from the four treatment groups at day 0 (top row – prior to any treatment), day 1 (2nd row – after initial treatments), day 25 (3rd row – at the conclusion of light treatment), and day 55 (bottom row – end of study). The left mouse, left flank (L, L) received no treatment; the left mouse, right flank (L-R) received PDN-only; The right mouse, left flank (R,L) receive PDN/Light and the right mouse, right flank (R,R) received

light-only. (B) Plot of relative volumes for bladder cancer xenografts over time following treatment with PDN/Light (red), light-only (green), PDN-only (blue), no treatment (black). (C) Histopathological Analysis of Tumor Tissue. Polarization detection as part of histological analysis for PDN in tissues excised from animals at the conclusion of the study receiving the following treatments: (top-left) - PDN/light; (top-right) – light-only; (bottom-left) – PDN-only; (bottom-right) – no treatment.